Effect of Pre-induced Plastic Strains on the Corrosion Behavior of Reinforcing Bar in 3.5 pct NaCl Solution

PRASANNA KUMAR BEHERA, PRVAN KUMAR KATIYAR, SUDHIR MISRA, and K. MONDAL

Reinforcing steel bar (rebar) is subjected to various levels of strains during service in reinforced concrete (RC) construction. This work aims at understanding the effect of pre-induced plastic strains on the corrosion behavior of a reinforcing steel bar (rebar) by doing electrochemical tests (electrochemical impedance and potentiodynamic polarization) in freely aerated 3.5 pct NaCl solution and cyclic salt-fog test. The interplay between the corrosion products and the corroding tendency of the strained rebars as a function of exposure time is analyzed. The plastic strains have strong effect on the composition of the rusts and polarization resistance of the rusted rebars.

I. INTRODUCTION

REINFORCING steel bars (rebars) used in reinforced concrete (RC) construction are subjected to different levels of elastic and plastic stresses and associated strains experienced during bending and cranking operations at construction sites, in the case of bent-up bars, stirrups or joints, or due to the action of structural loads in service. The former results in high plastic strain, but the effect is localized around the neighborhood of bends and hooks,[1–3] whereas the latter operations result in strain within its yield limit. However, the effect of elastic strain is more widespread along the length of the bars.[4] Though corrosion of the bars in concrete due to carbonation or chloride-attack has been actively studied,[5–8] the effect of such strains on the corrosion, both in terms of corrosion products and the rate, requires special attention.

Studies related to the corrosion of rebar in externally loaded RC members have reported higher crack-widths and deflections.[9–15] The combined effect of applied elastic stress and chemical attack on steels was investigated by Zhang et al.[16] in NaCl solution. The formation of micro-cracks in mortar due to external load has influenced the corrosion activity of rebar.[17] In one of their recent works, Li and Wu[18] have studied the degree of corrosion of rebars due to salt-fog exposure under the simultaneous action of tensile loads, and reported that the extent of corrosion increases in the stressed rebar.

If it is closely observed in most of the research articles relevant to the stress-induced rebar corrosion, rebar has been subjected to stresses and strains within its elastic region, leading to an increase in the corrosion susceptibility. Interestingly, the effect of elastic stress on the corrosion susceptibility has also been ascertained from the mechanochemical theory proposed by Gutman,[19] according to which the change in the electrode potentials ($\Delta\varphi_e^o$) of iron under the influence of the additional elastic stress is given by

$$\Delta\varphi_e^o = -\frac{\Delta P V_m}{zF} \qquad [1]$$

where ΔP is the additional elastic stress on the member (MPa), V_m is molar volume of the Fe (m^3/mol), z is valence of iron and F is Faraday's constant (96485 C/mol). From Eq. [1], it can be clearly understood that the higher the level of elastic stress, more negative would be the electrode potentials in the member, which would result in an increase in its corrosion susceptibility. However, this may not be true universally since potential is a thermodynamic factor, whereas rate of degradation is under the influence of kinetics of chemical/electrochemical reactions taking place on the surface of steel.

As mentioned earlier, apart from elastic strains, rebars are also subjected to considerable amount of plastic strains near bends and hooks (Figure 1(a)). The impact of corrosion on the mechanical properties of rebar subjected to such high tensile plastic deformation has been examined by Apostolopoulos and Michalopoulos.[20] They have studied the stress–strain behavior of a

PRASANNA KUMAR BEHERA and SUDHIR MISRA are with the Department of Civil Engineering, Indian Institute of Technology, Kanpur 208016, India. PRVAN KUMAR KATIYAR and K. MONDAL are with the Department of Materials Science & Engineering, Indian Institute of Technology, Kanpur 208016, India. Contact e-mail: kallol@iitk.ac.in
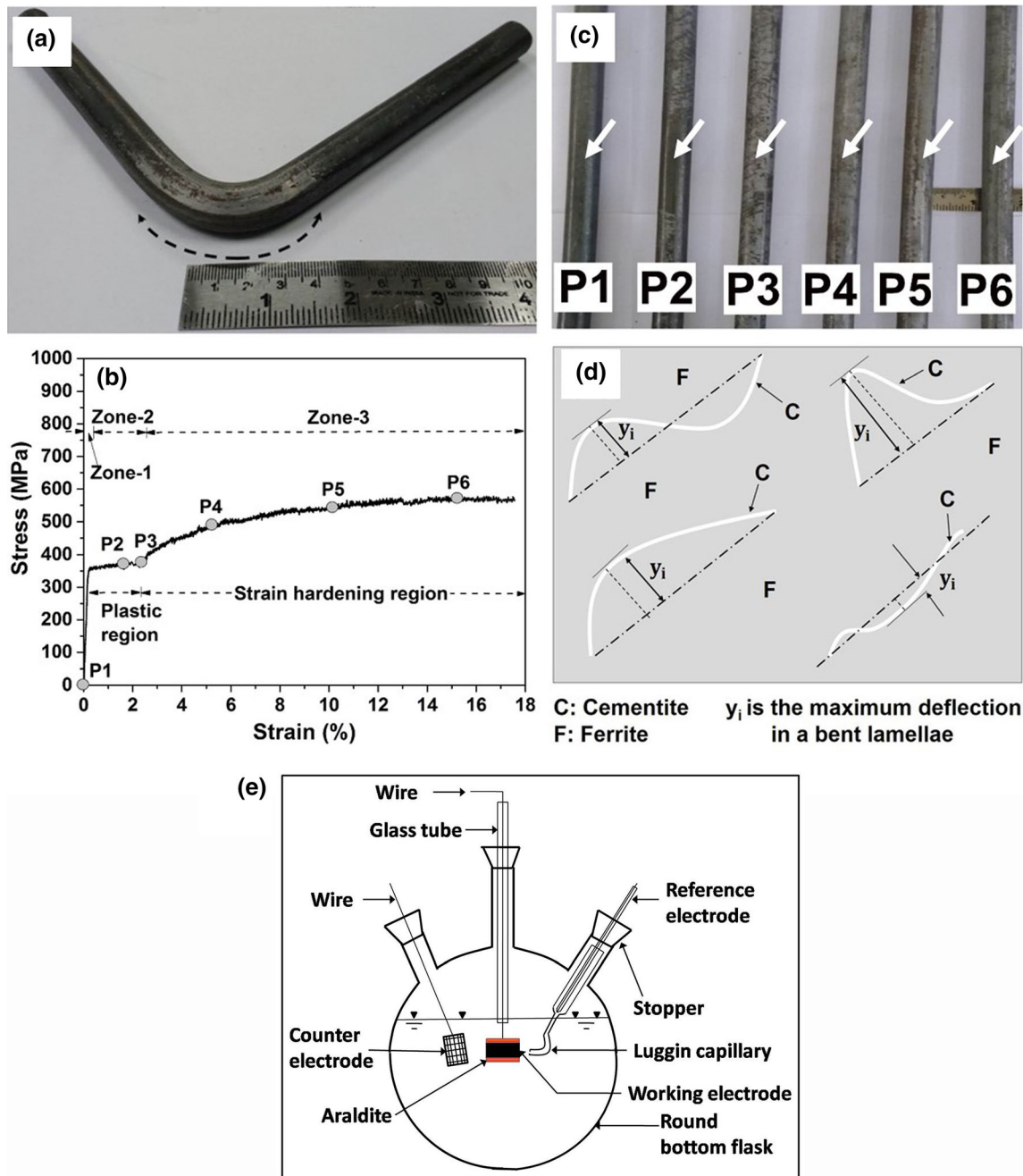
Fig. 1—(a) A typical 90 deg bend of plain reinforcing steel bar. (b) Typical stress–strain variation of the rebar used in the study along with the details of the notation followed for various levels of tensioning. (c) Rebars after pre-tensioning to various levels with specimen identity. (d) Method of determining the maximum deflection in the bent cementite lamellae from its initial position using FE-SEM images. (e) Schematic representation of the electrochemical test setup.

strained rebar after corroding it using salt-spray test and observed remarkable decrease in the strength and ductility of the steel due to the combined action of corrosion and plastic strains.

On the other hand, Zhang and Poursaee[21] have reported that steel specimens under tensile loads passivate more rapidly in chloride-free pore solution compared to those under compressive and no-loading conditions. Due to rapid passivation initially, steels under tension tend to form more protective passive films, which has led to the recording of lower current densities in the later stages. However, when the pore solution is contaminated with chlorides, an opposite behavior in the tensioned steels has been observed. In addition, they have also reported that the effect of tensile or compressive stresses in steel is more significant than the influence of the passive layer in protecting the steel from corrosion in the presence of chlorides.

From the brief review listed above, it is clearly evident that very limited understanding on the impact of pre-induced plastic strains on the corrosion behavior of rebar is available in the literature. Moreover, the

research articles addressing the implications of plastic strains have presented the behavior of the passive films formed on steel in concrete pore solution[22,23] rather than the inherent nature of the metal substrate underneath the film. This would, particularly, become crucial from the viewpoint of RC construction. The steel bars procured for construction are usually very long, and in bent form while they are brought to the construction sites (to facilitate the transportation of long bars). Later, they have to be cut, bent to different shapes and stored at sites before being placed in position for structural purposes. Such bent-up bars, bends, hooks and stirrups are very common in civil engineering structures, in which plastic deformation is inevitable. Therefore, rebar would be exposed to atmosphere in plastically strained condition before concrete is placed around them. There could be a situation of an aggressive marine environment (enriched with chlorides) near storage sites. Unlike the elastic strains that are induced in rebar after casting an RC member and subjecting it to external service loads, the plastic strains in the steels at the bent portion are induced prior to concreting. Therefore, in such cases, they would be exposed to aggressive Cl$^-$ ions (example: marine exposure) which may result in predominant rust formation before passivating in high pH environment of concrete. It is important to mention that though codes and standards specify to avoid the contact of rebar with aggressive agents during storage, it is highly impractical to have rust-free rebar at construction sites. Practitioners often use some crude remedies to remove the rust on bar (cleaning with wire-brush or using Clark's solution, etc.). Such practices could have long-term implications as they affect the surface condition of rebar by inducing scratches or defects. Thus, understanding the corrosion behavior of the strained rebar in a chloride-contaminated environment (example: 3.5 pct NaCl solution) is of paramount importance to highlight the special care and attention required to create and handle bent rebars.

Furthermore, depending on the angle of bend and the diameter of the mandrel used, the extent of plastic strains in a rebar could vary over a large range. One interesting aspect arising on the account of plastic pre-straining at the bends is the damage that occurs to the mill-scale, which is a thin adherent oxide layer on the surface of a rebar.[24] As shown in Figure 1(a), at the location of the bend (a trial test in the present work), the scale has been damaged on account of plastic deformation (shown by dotted arrowhead), whereas the scale on the unstrained portion has remained intact. Therefore, for a meaningful comparison between the corrosion behavior of the strained and unstrained rebars, surface dissimilarity arising on account of mill-scale should also be taken into consideration. Moreover, plastic strains could also result in significant changes in the microstructure of the steel. The previous studies,[25–27] reporting the changes in the microstructure of carbon steel due to strain, are mostly related to its warm deformation. In such cases, changes occur in steel before the final product (rebar) is made. However, due to construction operations, plastic strains are induced in the final product itself, and hence, the associated changes could be different from that of warm deformation.

Interestingly, critical examination of such changes has never been studied.

To acquire a comprehensive idea of corrosion behavior of strained rebar in an aggressive marine environment, apart from obtaining the electrochemical information of diffused double layer formed at the interface, it is equally important to examine their actual corrosion behavior as a function of time. Thus, two clear objectives have been finalized as part of the study. To achieve these objectives, the experimental program has been organized into two phases as shown in Table I. While the electrochemical tests on bare rebar specimens are part of Phase-I, Phase-II deals with the cyclic salt-fog tests and the changes in their electrochemical behavior as a function time. Thus, both the Phases-I and II have been aimed at extracting the electrochemical information of the strained steel in 3.5 pct NaCl solution.

On an independent note, it is known that depending on the availability of oxygen and moisture, a wide range of corrosion products can form on reinforcing steels.[24,28] Several researchers, including the present authors, have reported the systematic changes in corrosion products formed on rebar steels in various exposure conditions.[24,28–32] It has also been established that the ratio of stable Goethite (α-FeOOH) to the sum of the proportions of Lepidocrocite (γ-FeOOH), Akaganeite (β-FeOOH) and Magnetite (Fe$_3$O$_4$), i.e., α/γ^* indicates the protective ability of rust,[32–35] and can serve as an effective parameter to assess the corrosion tendency of rusted steels.[32] The relationship between the corrosion products formed during exposure and the electrochemical properties of rusted mild steel has been reported by Choudhary et al.[32] However, the nature of corrosion products formed and their gradual transformation, which are likely to be affected by the amount of plastic strains in the steel, have not been documented.

To provide a fresh perspective to the problem, the present research focuses on examining the corrosion behavior of the rebars having various extents of pre-induced plastic strains not only from an electrochemical viewpoint, but also from the nature of the corrosion products formed on their surfaces. Since the nature of the corrosion products formed on steel serve as a fingerprint of the corroding system, efforts have been made to obtain the composition of the rust and correlate it with the changes in the electrochemical behavior. It is expected that a study of the effect of plastic strain on the interplay between the electrochemical properties and the composition of rust would help to better understand the corrosion behavior of the very important component in reinforced concrete structure, rebar.

Few aspects related to the test period in cyclic salt-fog tests are worth mentioning in this context. In comparison to other accelerated corrosion tests, the level of corrosion that rebar undergoes in a given time period in cyclic salt-fog test would be very high. This is mainly due to the critical combination of the temperature, humidity and high Cl$^-$ content inside the chamber.[36] Thus, in salt-fog tests, the properties of rust (such as composition, morphology and protective ability) and the associated electrochemical properties of rusted steels

change very rapidly. A close observation of the published literature[31,32] would clearly indicate that the changes in the rusted steel would saturate in 30 days due to the stabilization of corrosion products, after which the rust starts detaching from the rebar due to its flaky nature. Thus, an exposure period of 30 days is considerably high in salt-fog tests. Therefore, in the present study, the experimental investigation carried out as part of Phase-II is limited to 30 days. In such case, the time-dependency of the corrosion products and the corresponding electrochemical behavior of rusted rebar are the important aspects that need to be addressed to develop a comprehensive understanding. Accordingly, tests in Phase-II have been aimed at estimating the polarization resistance of the rusted rebar and correlation with its corrosion products after exposing to different time-periods in the chamber.

To avoid the usual crevice corrosion at the ribs of a corrugated bar, plain round bars were used in this research. Differentiating the corrosion due to plastic strain from the crevice formation at the ribs of a usual high tensile corrugated bar is impractical as both the effects are coupled. Hence, to avoid this obscure formation of crevice at ribs, steel bars without ribs were chosen for the study. It is worth mentioning that in principle, the carbon content of both plain rounds and ribbed bars is nearly same, and their basic microstructural constituents comprise similar phases (ferrite and pearlite colonies).[37,38] Hence, though the corrosion behavior of bent ribbed and plain bars could be slightly different, the fundamental understanding related to the effect of strain remains same in both the cases. Furthermore, understanding the mill-scale related effects on the plain bar is easy.

Electrochemical measurements on a series of strained rebar specimens containing various levels of plastic strains in freely aerated 3.5 pct NaCl solution include open circuit potentials, electrochemical impedance spectroscopy and potentiodynamic tests. Finally, the paper presents the variation in the protective abilities and the electrochemical behavior of the rusted and strained rebars in 3.5 pct NaCl solution as a function of time.

II. EXPERIMENTAL DETAILS

A. *Specimen Preparation and Metallography*

Specimens for the two phases of experiments were obtained from 16 mm rounded mild steel, consisting 0.20 pct C, 0.16 pct Si, 0.46 pct Mn, 0.05 pct P, 0.11 pct S, 0.04 pct Cr, 98.7 pct Fe (all are in weight pct) along with other trace elements. The tensile stress–strain behavior of the rebar was determined by testing three 500-mm-long specimens as per IS 1608:2005,[39] and a typical plot is shown in Figure 1(b). It has been found that the material has yield and ultimate strengths of 350±2 and 565±5 MPa, respectively, with the lower yield point at 0.2 pct strain level. Details of the extent of tensioning used in the study and the corresponding notation followed in this paper are given in Figure 1(b). The bars were strained to the required levels in a

Universal Testing Machine (Tinius Olsen Model 2000SL) at a strain rate of 0.0025 s^{-1}. The final diameters after tensioning were obtained using Eq. [2], and found to be in good agreement with the physical measurements carried out using Vernier calipers.

$$\frac{d_i - d_f}{d_i} = \mu_s * \frac{\delta l}{l} \qquad [2]$$

where d_i and d_f are the initial and final diameters of the rebar, respectively, $\frac{\delta l}{l}$ is the plastic (or residual) strain in the strained rebar and μ_s is the Poisson's ratio of steel, which is taken as 0.30.[40] While the specimen P1 was not strained for reference, the specimens, P2–P6, were strained to a level of 1.5 pct, 2.2 pct, 5.0 pct, 10.0 pct and 15.0 pct, respectively, and are pertaining to various zones in the stress–strain curve as shown in Figure 1(b). Figure 1c shows the unstrained and strained rebars used in the study.

The total number of bars strained up to a certain level was four, and out of which one rebar was used to generate specimens for each of the following tasks in the work: (a) metallographic observations, (b) electrochemical measurements on bare specimens in phase-I, (c) to obtain the corrosion products in phase-II, and (d) electrochemical measurements on rusted specimens in phase-II. For each task, triplicate specimens having a thickness of 5 mm were cut from the strained and unstrained rebars (P1–P6). These specimens were taken from the central portions of rebar to avoid any end effects arising on account of gripping in the tensile testing machine. The specimens were cut from the bars using a slow-speed automated saw. During the cutting process, coolant was also used to avoid heating of the specimen. Thus, the chances of stress relaxation in the specimens due to the increase in temperature were minimized. For microstructural observations, the cross-sections of the specimens were mechanically ground using emery papers up to 1200 grit size followed by cloth-polishing using alumina suspension, and, finally etched with 3 pct Nital. The lamellae structure within the pearlite was examined using FE-SEM (Nova NanoSEM 450) at an accelerating voltage of 20.00 kV. In all the steels, the deflections in various cementite lamellae were measured at several locations using the scaled FE-SEM micrographs.

The physical process of deformation in ferritic-pearlitic steels during tensile testing depends on the mechanical properties of individual phases (ferrite and cementite). During plastic deformation, load transfer from ferrite to cementite occurs due to the inherent differences in their mechanical properties.[41] This leads to significant localization of stress in cementite, which would ultimately cause the bending and/or fragmentation of the lamellae. Earlier work by Sharma *et al.*[42] has clearly shown that the deformation without fracture could align the cementite lamellae in fully pearlitic steel (0.7 wt pct rail steel) along the loading axis as well as bending of the cementite as observed during systematic reciprocating wear analysis. In the present work, since the loading is in plastic range, the stresses could definitely lead to the bending of the cementite. Hence,

Table I. Details of the Experiments Carried Out in the Present Study

Phase	Experiments	Objective
I	electrochemical tests in freely aerated 3.5 pct NaCl solution	• to obtain the charge-transfer resistances (R_{ct}) and the corrosion current densities (i_{corr}) of the unstrained and strained rebars
II	cyclic salt-fog tests (3 hours of wetting and 9 hours of drying)	• obtaining the following information related to the corrosion products formed on the unstrained and strained rebar specimens at the end of different exposure periods (5, 10, 20 and 30 days) •Type and proportions of various corrosion products • R_p behavior of the rusted rebars using linear polarization tests

the pearlite colonies near the periphery of the specimen (outer edge) were examined to assess the deflections of lamellae. This was particularly done to maintain the uniformity in selecting the locations for acquiring micrographs. Further, eight different spots spaced at an interval of 45 deg ($= 360$ deg/8) on the circumference of the rebar were chosen. At each spot, micrographs at four different locations, each focusing a particular pearlite colony, were acquired. Thus, a total of 32 pearlite colonies were examined in each rebar. In these colonies, straight lamellae were not considered for calculating the deflections in cementite phase. However, all the lamellae, which had undergone bending either moderately or severely, were considered in estimating the average deflection.

The line joining the ends of a given lamella was considered to be its initial position, and the deflections were measured with respect to this line (Figure 1(d)). The maximum deflection of a cementite lamella was taken to be the representative measure of the effect of plastic pre-tensioning. The average of all such maximum deflections obtained from various lamellae was used for comparison among the strained steels. It would be worth mentioning that the steel specimens used in the study were prepared from 12-m-long rebars belonging to the same lot, and have similar composition. Therefore, changes in their microstructures could solely be attributed to the extent of plastic pre-tensioning.

B. Electrochemical Tests

1. EIS and Polarization Studies

The electrochemical tests on the strained rebar specimens in Phase-I were carried out to understand their corrosion behavior in freely aerated 3.5 pct NaCl solution. Apart from the control specimen (P1, 0 pct strain), the specimens pertaining to five different levels of tensioning (P2–P6) were tested. The curved surfaces of the rounded specimens were having mill-scale in either fully intact condition (P1), or partially or completely damaged condition depending on the level of strain (P2–P6) (Figure 1(c)). The usual metallographic polishing before electrochemical testing was avoided to capture the macro-cell galvanic effects. However, to understand the influence of damaged mill-scale in facilitating macro-cell effects in the specimens pertaining to zone-2, the P2 specimens without having scale on their surface were also tested. To avoid any unwanted

damage to the specimen while removing the scale, the surface was polished using ultra-fine emery paper Grit-800. The surfaces of the specimens were cleaned ultrasonically in acetone before performing the tests.

The necessary connections were made on the cross-sections of the specimens, which were later coated using standard epoxy lacquer (Araldite). Thus, the interaction of cross-section with the electrolyte was avoided using Araldite epoxy, and the curved surface portion of the test specimen was exposed to electrolyte. This was done to perfectly simulate the chloride-attack phenomenon in rebar, which happened on the curved section, but not on the cross-section of rebar. A schematic representation of the test setup is shown in Figure 1(e).

Tests were carried out in a round-bottom cell using Parstat 2263 system at room temperature. Volume of the electrolyte in all the tests was 400 ml. Three-electrode setup was used where the specimens, platinum wire mesh and saturated calomel electrode (offset potential with respect to SHE: $+ 0.242$ V) were the working electrode, counter electrode and reference electrode, respectively. Luggin capillary facilitating in directing the conductive path between working and reference electrodes was used (Figure 1(e)). Furthermore, the test setup enabled proper sensing of current and voltage as no major challenges with respect to the blockage of field lines among individual electrodes were foreseen since the electrolyte was highly conductive (3.5 pct NaCl solution). Initially, the specimens were immersed in the electrolyte for 1 h to stabilize the open circuit potentials (OCP). Then, to obtain the charge-transfer resistances using EIS at free corrosion potentials, the specimens were subjected to AC perturbation of 10 mV. Frequency was swept from 100 kHz to 10 mHz. Results of EIS were modeled and analyzed using an appropriate equivalent electrical circuit (EEC) model available in ZsimpWin software (Princeton Applied Research).

Dynamic polarization behavior was studied by subjecting the specimens to over-potentials ranging between $- 250$ and $+ 300$ mV from their respective OCPs. The negative and positive potentials with respect to OCP enabled to record the cathodic and anodic polarization curves of the specimens, respectively. A constant scan rate of 0.5 mV/s was used in all the tests. Corrosion current densities (i_{corr}) of the steels were calculated using Tafel extrapolation in case of systems which had exhibited either activation or mixed polarization

behavior. In case of corroding systems in which either spontaneous passivity was noticed, passive current densities corresponding to the onset of passivity (where change in the slope of the anodic part occurred) were estimated. Further, corrosion rates of the specimens were calculated using Eq. [3] as per ASTM G102.[43]

$$\text{Corrosion rate (mm/y)} = \frac{(3.23 \times 10^{-3}) \times (i_{\text{corr}}) \times (EW)}{\rho}$$

[3]

where i_{corr} is corrosion current density in μA/cm^2, EW is the equivalent weight of iron considering valence to be 2 (= 27.92), ρ is the density of the steel (= 7.86 g/cm^3). Three specimens were tested for each strain level to ensure repeatability, and average was used for comparative assessment.

2. Salt-Fog Tests and Subsequent Electrochemical Measurements

Tests in Phase-II (Table I) were carried out to examine the corrosion behavior of the rebar specimens as a function of time by placing them in a cyclic salt-fog test chamber and accelerating the corrosion. Based on the results in Phase-I as explained in the following sections, only the unstrained (P1) specimen, and the specimens prepared from P3 and P5 were tested in this phase.

A closed chamber conforming to ASTM B117[36] was used in the study with 3.5 pct NaCl, and the specimens were exposed to exposure periods of 5, 10, 20, and 30 days. Throughout the test period, the specimens were subjected to two cycles per day, each comprising 3 h of wetting and 9 h of drying periods. The chamber temperature was around 35 °C after reaching the steady-state conditions. Six different specimens for each combination of straining and exposure period were drawn, and while three of these were used for spectroscopic analysis, the other three were used for obtaining the polarization resistance (R_P) by carrying out linear polarization of corroded specimens without disturbing the rust by careful handling.

Electrochemical measurements were carried out on the corroded specimens at the end of each exposure period. Measurements included the OCP evaluation and measurement of R_P from linear polarization tests in 3.5 pct NaCl solution. Linear polarization measurements were taken after stabilization of OCP in a potential range of ± 20 mV at a scanning rate of 0.166 mV/s. However, linear portion between ± 5 mV was only used to calculate the polarization resistance (R_P). At the end of a given exposure period, rust samples were collected from the corresponding corroded specimens using a spatula, and were immediately prepared for Fourier Transform Infrared (FTIR) analysis. Apart from obtaining the qualitative information of corrosion products from FTIR spectra, quantitative analysis was also performed using the Beer-Lambert's law, i.e., the absorbance is equal to log (100/T), where T is the transmittance (pct), as suggested in earlier studies to determine the relative fractions.[24,32,38].

Fig. 2—(a) through (g) Typical FE-SEM micrographs for the as-received (a) and (b), and P2–P6 (c) through (g), respectively, and, (h) the average maximum deflection of the bent lamellae in the strained specimen with different levels of pre-induced plastic strains. Pearlite colony (P), cementite (C) and ferrite (F). (1) Loading direction is perpendicular to the plane of the micrographs (Z-axis); (2) referring Figure 1(d) to ascertain the bending of the lamellae and the maximum deflection measurements.

III. RESULTS AND DISCUSSION

A. Metallography

The change in the surface appearance of the strained rebars clearly confirms the damage occurred to the mill-scale as shown by arrowheads in Figure 1(c). Hence, the actual surface conditions of differently strained portions in a bend as indicated in Figure 1(a) have been perfectly simulated in this study. As can be seen from Figure 2(a), in general, the steel used in the study has ferritic-pearlitic microstructure. Though the orientations of different lamellae among pearlitic colonies are different, the cementite lamellae are oriented in a similar way in a particular colony, and relatively less bent (almost straight). Figures 2(b) through (g) shows the typical high-resolution micrographs of different steel specimens (P1–P6). It can be seen that in general, as the amount of plastic strain increases, the bending in the cementite lamellae also increases (Figures 2(b) through (g). The average maximum deflection of the lamellae obtained in various strained steels is shown in Figure 2(h). The unstrained specimen (P1) also shows some deflection in pearlite, which can be attributed to the rolling process during the manufacturing of bar. However, with the introduction of permanent plastic strain (P2–P6), bending of the lamellae increases.

It could be pointed out that the orientation of pearlitic colony with respect to the loading axis during the tension test is also an important factor. In this context, it can be seen that lamella of some of the unfavorably oriented pearlite colonies get deformed to much greater extent, and this is clear from the micrographs of specimens with higher level of plastic strains (P4–P6) in Figures 2(e) through (g) and Figure 2(h). A close examination of the lamellae for the specimens P4–P6 at some locations (shown by dotted arrowheads) in Figures 2(e) through (g) clearly confirms the local fracture. While severely bent and fractured lamellae are observed in the specimen P5 (Figure 2(f)), extreme straining in specimens P5 and P6 caused significant kinking in the cementite lamellae (Figures 2(f) through (g)). In the latter, severe bending and fracture in the lamellae are seen in the form of blunted fibers at some locations (shown by dotted circle in Figures 2(f) and (g)). Thus, it can be concluded that plastic pre-straining the specimen has resulted in significant changes in the shape and extent of bending in the lamellae present in their microstructures.
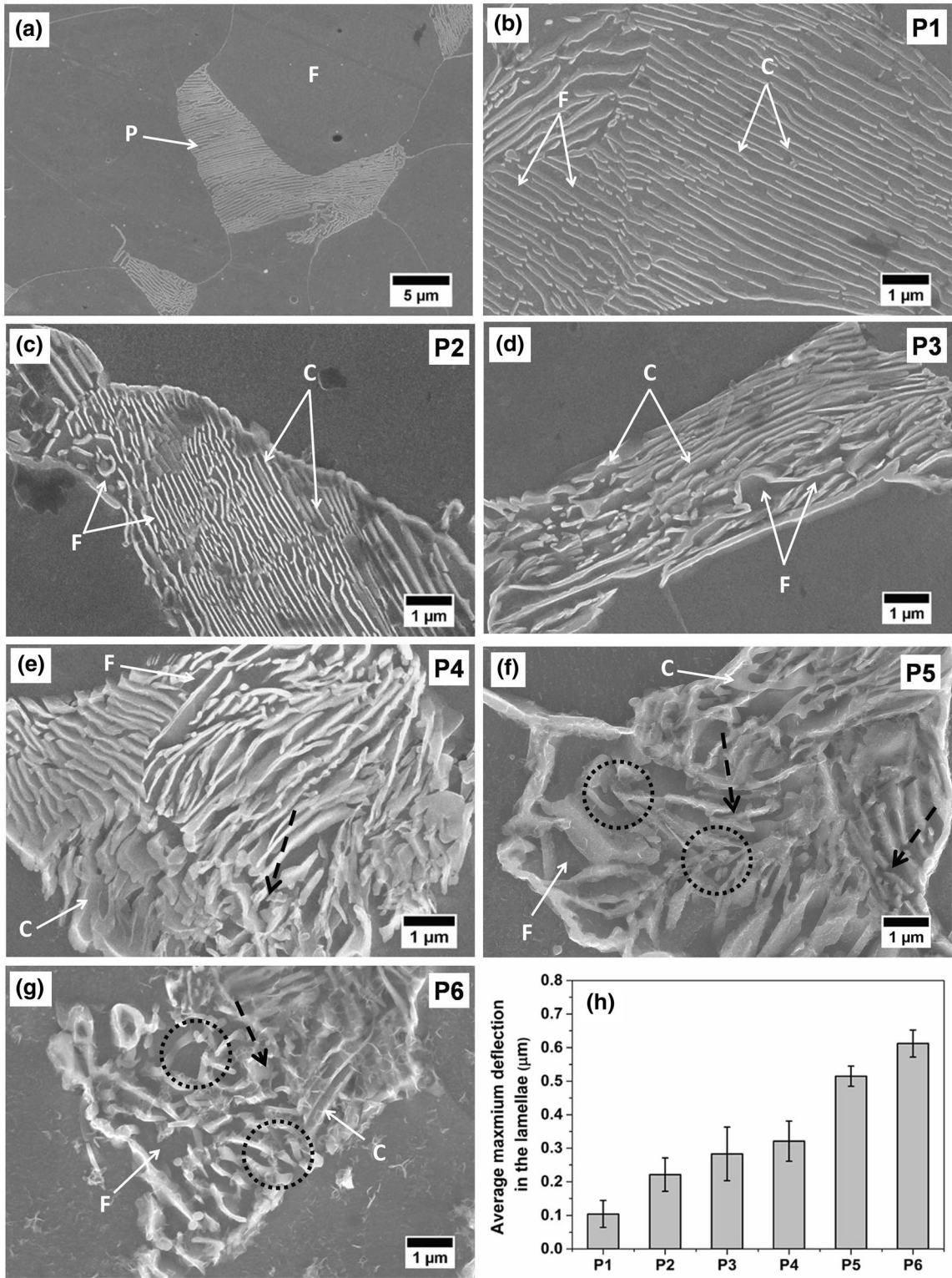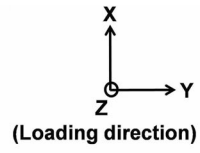
B. Electrochemical Behavior of the Strained Rebars

Variation of OCP for all specimens in 3.5 pct NaCl solution is shown in Figure 3(a). It can be seen that the OCP has stabilized at values given in Table II almost at the same time for all the specimens. In general, it can be seen that the stabilized OCP values for the strained steels are more negative than that of the unstrained steel, and the values become more negative as the level of the plastic strain in the specimen increases. This can be attributed to the increased activity of the metallic portion arising on account of changes in the surface and the structure of the pearlitic colony as indicated in Figures 2(b) through (g). It may also be pointed out that an increase in the dislocation density has been reported with the increase in strain,[40] which could also explain the trend observed in this study. It is worth reiterating that the OCP is the potential indicating the steady-state potential where the cathodic reaction (here it is oxygen reduction in neutral solution) and anodic reaction (dissolution of Fe) rates are equal at open circuit condition. Therefore, due to the inherent increase in
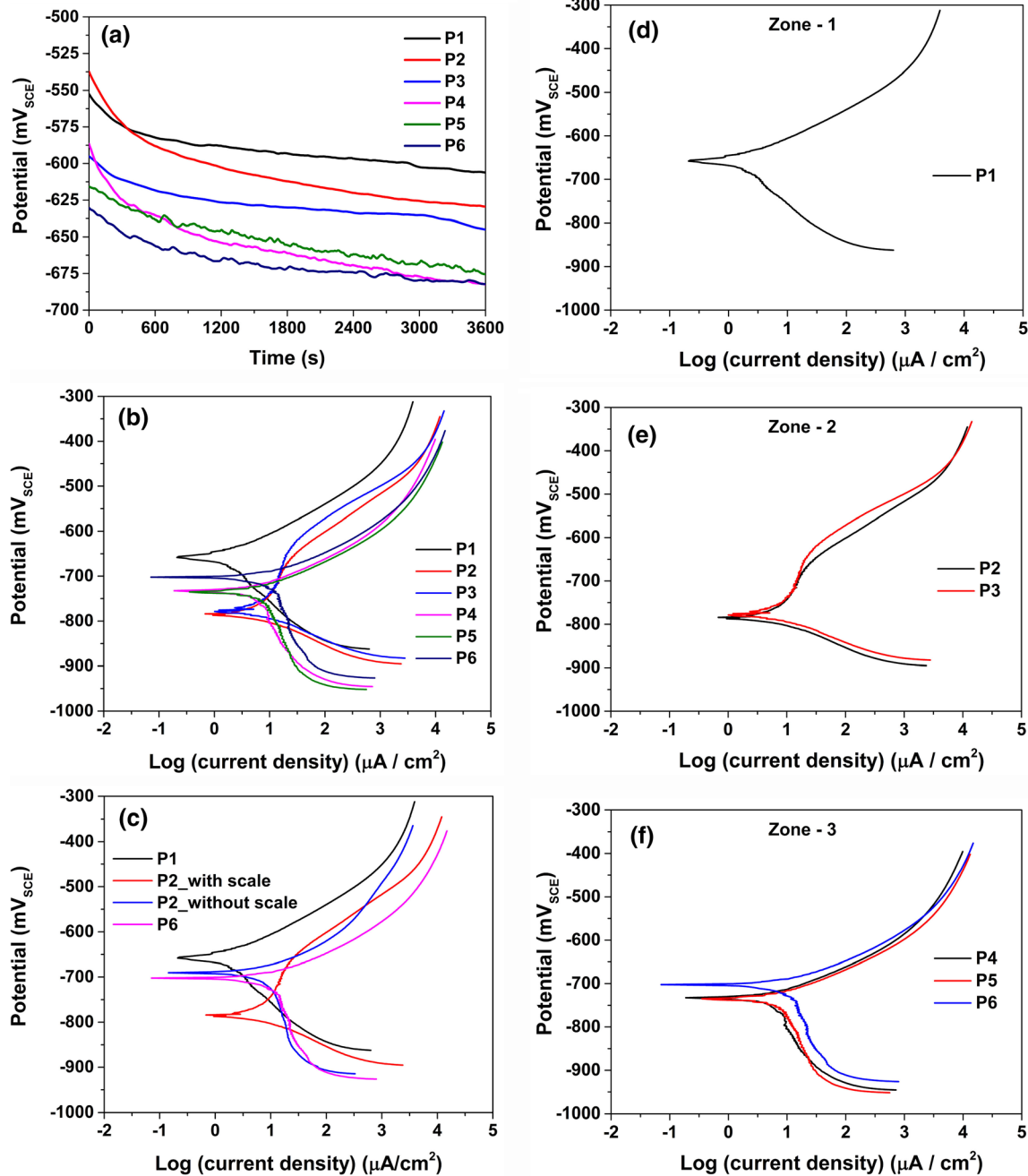

Fig. 3—(a) OCP variation with time. (b) Potentiodynamic polarization plots of the specimens in 3.5 pct NaCl solution. (c) Comparative polarization behavior of P2 specimen with and without the scale in 3.5 pct NaCl solution along with P1 and P6. (d–f) Polarization behavior of the specimens pertaining to zones-1, 2 and 3 in 3.5 pct NaCl solution.

Table II. Electrochemical Parameters of the As-Received (P1) and Strained (P2–P6) Rebar Specimens Extracted from the Potentiodynamic Polarization Tests in 3.5 pct NaCl Solution

Specimen	OCP (mV_{SCE})	E_{corr} (mV_{SCE})	β_a (mV/decade)	$-\beta_c$ (mV/decade)	i_{corr} ($\mu A/cm^2$)	Corrosion rate (mm/y)
P1	− 606	− 667	64	110	1.64	0.0188
	(6)	(8)	(9)	(12)	(0.37)	(0.004)
P2	− 644	− 780	*	55	4.56**	0.0523
	(8)	(7)		(8)	(0.16)	(0.001)
P3	− 635	− 767	*	46	5.01**	0.0574
	(4)	(8)		(11)	(0.27)	(0.003)
P4	− 689	− 740	45	155	7.11	0.0815
	(8)	(5)	(7)	(14)	(0.32)	(0.003)
P5	− 685	− 728	50	190	9.57	0.1098
	(4)	(8)	(9)	(8)	(0.52)	(0.006)
P6	− 680	− 713	53	320	12.52	0.1436
	(8)	(9)	(4)	(14)	(0.36)	(0.004)
P2_without scale	− 663	− 675	27	340	8.78	0.1007
	(7)	(6)	(10)	(18)	(0.45)	(0.002)

Standard deviation is mentioned in brackets.
*Showing spontaneous passivity.
**Passive current densities for P2 and P3.

the dislocation density in steel with the increase in pre-strain, more negative OCP has been obtained.

Dynamic polarization plots of the strained specimens as well as the unstrained specimen in freely aerated 3.5 pct NaCl solution are presented in Figure 3(b), and the typical polarization response of P2 specimen without the damaged scale on its surface is shown in Figure 3(c) (along with other plots to facilitate comparison). The polarization responses of the specimens pertaining to each individual zone are shown in Figures 3(d) through (f).

Electrochemical parameters, such as corrosion potentials (E_{corr}), corresponding current densities (i_{corr}) and the corrosion rates of the strained specimens, are also summarized in Table II along with the anodic (β_a) and cathodic (β_c) Tafel slopes. It can be clearly inferred from Figures 3(b) through (f) that the polarization behavior of the rebars is affected by the level of plastic strain, which is related to the extent of tension induced in the bars, and also the level of damage to the mill-scale (Figure 1(c)). As stated earlier, mill-scale is a flaky oxide layer formed on the surface of rebars during hot-rolling operation in mills.[24,44] From purely electrochemical viewpoint, it is cathodic to steel.[44] Mill-scale could cause large ohmic loss due to its high resistivity, and has been reported to be loose and contain defects and micro-cracks.[44,45] Nevertheless, it acts as physical barrier to the deleterious agents, and could also delay the onset of corrosion.[44,45] Due to plastic pre-tensioning, the scale on the rebar has undergone damage, as shown in Figure 1(c). While the P1 specimen (zone-1) has shown activation-controlled behavior with slight signature of passivity at around 2 to 3 $\mu A/cm^2$ current density (Figure 3(d)), the P2 and P3 (zone-2), have been observed to exhibit clear spontaneous passivity, and their systems are not guided by concentration polarization (Figure 3(e)). The spontaneously passivating nature

of the system in P2 and P3 (zone-2) is due to the macro-cell galvanic effect as explained in the subsequent paragraphs. The cathodic branch in case of the specimens P4, P5 and P6 (zone-3) is mixed-controlled with increase in slope in the cathodic portion due to influence from diffusion-controlled effect (Figure 3(f)). However, the anodic portion does not show any signature of passivity in the specimens of zone-3 (Figure 3(f)). In addition, the E_{corr} of the P1 (zone-1) is much higher as compared to those of P4–P6 (zone-3). Furthermore, the anodic current density of the P1 (zone-1) is also almost two orders of magnitude less than those of the P4–P6 (zone-3) (Figure 3(b)), considering the fact that P1 and P4–P6 show active anodic dissolution.

Closer examination also reveals that the specimens P2 and P3 show slight passivity (Figure 3(e)) as compared to other specimens. The respective passive current densities are listed in Table II. Interestingly, the breakdown in both the P2 and P3 specimens has occurred at nearly same potentials ($\sim$ − 650 mV_{SCE}) after passivation. The change in the polarization behavior can be attributed to the nature of the surface in different specimens. The fully covered metal with mill-scale in the unstrained P1 shows active behavior, whereas the specimens P2 and P3, which are taken from the yield zone (Figure 1(b)), show spontaneous passive behavior. Since the P2 and P3 are from the yield zone, the passivity is surely related to (a) the Lüders band formation, which is accompanied with the simultaneous release of pinned dislocations in the Cottrell atmosphere of mild steel, and also (b) to the presence of damaged mill-scale on the surface. With increase in pre-straining in the plastic portion of the tensile plot (zone-3 in Figure 1(b)), the steel show active behavior again with mixed-controlled corrosion behavior having larger effect from concentration polarization for the oxygen reduction reaction ($\frac{1}{2}O_2 + H_2O + 2e^- \leftrightarrow 2OH^-$). The very

change in corrosion control in the strained specimens is characterized by the gradual shift of the plots to higher current side (Figures 3(b), (d) through (f)).

Though reasonable low scan rate (0.5 mV/s) has been used in the present case, there is difference in the OCP and E_{corr} values, however, within 100 mV. In general, the E_{corr} values of the strained specimens (P2–P6) have been observed to be more negative than the unstrained specimen, P1, which indicates thermodynamic instability of the former specimens as a group (Table II and Figures 3(d) through (f)). Interestingly, the E_{corr} of the specimens pertaining to zone-2 (P2 and P3) are more negative as compared to those of zone-3 (P4–P6). Moreover, at very high levels of plastic strains in zone-3, the E_{corr} has moved in positive direction, or in other words, among the strained specimens, as the amount of plastic strains increased, E_{corr} has shifted to more noble values (Figure 3(b)). This trend of ennoblement among the strained specimens can be explained based on a careful understanding of two factors, i.e., dislocation density and macro-cell galvanic activity between scaled and un-scaled portions.

The specimens P2 and P3 are characterized with partially damaged mill-scale (Figure 1(c)), which results in greater tendency for the macro-cell galvanic activity between scaled and un-scaled portions. Both the dislocation density and the macro-cell activity aggravate the thermodynamic instability in these specimens (P2 and P3), and hence, more negative E_{corr} has been obtained. This macro-cell activity could also attribute to the appearance of passivity in P2 and P3 (Figure 3(e)). At higher anodic potentials, the exacerbated thermodynamic instability (due to macro-cell activity) would contribute in the formation of oxide layer on the rebar surface, which eventually reflected in the form of passivity in P2 and P3 (zone-2) specimens (Figure 3(e)). As the amount of plastic strain increases (higher levels of pre-tensioning), the dislocation density also increases. But the possibility of macro-cell formation reduces due to complete removal of the mill-scale on the surface. In case of P4 and P5 specimens, relatively less presence of mill-scale reduces the effect due to macro-cell formation (Figure 3(f)). As far as the P6 specimen is concerned, the scale has been totally removed leading to the exposure of fresh metal (Figure 1(c)), which shows the behavior of the strained steel without the mill-scale. In this case, the comparison of E_{corr} values of the as-received P1 and heavily strained P6 indicates that the E_{corr} of the latter is lower than that of the former. This is understandable since the first one is completely covered by mill-scale (Figure 1(c)), and the latter is completely free of mill-scale due to heavy straining. The lower E_{corr} in the P6 with respect to the P1 can be attributed to the higher strain energy because of higher dislocation density (Table II and Figure 3(b)).

In general, the damaged mill-scale promotes local interactions between the scaled and the un-scaled portions (as observed in the zone-2 specimens). While the scaled portions tend to support more oxygen reduction reactions, anodic dissolution occurs at the un-scaled (bare) portions.[46] This translates the system into thermodynamically (more) unstable condition, as

observed by more negative E_{corr} values in the zone-2 specimens (P2 and P3) as compared to the other specimens.

The above understanding related to the influence of damaged mill-scale on the thermodynamic stability of the P2 and the P3 specimens (zone-2) can be better understood in Figure 3(c), which shows the polarization behavior of the P2 without the damaged mill-scale along with the results of the P1, the P6 and the P2_with scale. From Figure 3(c), it can be inferred that the E_{corr} value of the P2_without scale is around − 675 mV$_{SCE}$, which is higher than the E_{corr} of the P2_with scale and P6 specimen, which are − 780 and − 713 mV$_{SCE}$, respectively. This confirms that the increased thermodynamic instability in the P2_with scale specimen is due to its macro-cell effects arising on account of damaged mill-scale. Furthermore, there is no passivity in P2 when the damaged scale was not present on its surface (Figure 3(c)), and this confirms that the passivity in the P2 specimen with mill-scale is due to the local corrosion cell formation. Thus, in the zone-2 specimens, both the inherent tendency to corrode due to the increase in dislocation density and the partially damaged mill-scale contribute to the formation of corrosion products. Hence, the surface of the specimen would have more covering effect by the corrosion products locally, which has been reflected in the form of passivity at higher anodic potentials (Figure 3(b)).

Furthermore, there is a similarity in the anodic branches of the polarization plots of specimens P1, P4, P5, and P6, considering the fact that they show active anodic dissolution (Figure 3(b)). However, it has already been mentioned that the anodic current density of the P1 is almost two orders of magnitude less than those of the P4–P6 specimens. Moreover, this can be comprehended from the anodic slopes of the polarization curves of the specimens (Table II). The anodic slope (β_a) of P1, which is the specimen having sound cover of mill-scale, as mentioned in Table II, has been obtained to be higher than those of the P4–P6 specimens not having the scale (Table II). This essentially implies that higher potential difference is required in case of P1 than in P6 to cause a unit change (decade) in the anodic current density. Thus, it can be understood that the oxidation rate in the P4-P6 is higher than that in P1 due to the accumulation of residual strain and the reduced inhibiting action of the mill-scale toward polarization.

The cathodic slopes (β_c) of the P2 and P3 (zone-2) specimens are less than that of P1 (zone-1) (Table II). It means relatively less over-potential is required to cause unit activity in P2 and P3 (zone-2). This signifies the tendency for the formation of local corrosion cells on the P2 and P3 specimens due to uneven presence of mill-scale on their surfaces (Fig 1c). This can be better interpreted from Figure 3(c), which shows the polarization response of the P2 specimen in which the damaged mill-scale was removed. The cathodic slope of the P2 in the absence of scale (P2_without scale in Table II) has increased significantly, and it is similar to the cathodic slope of the specimen P6 (Figure 3(c)).

When the damaged mill-scale was removed (i.e., in P2_without scale specimen), there is a larger influence of

oxygen reduction reaction, which has reflected in the form of mixed-control behavior with larger effect from concentration polarization (Figure 3(c)). This is due to the increased cathodic activity on the exposed cementite (damaged due to straining) of P2 specimen (without scale) on account of pre-strain (increased cathodic slope in P2_without scale as compared to P2_with scale (Table II)). It means the damaged mill-scale in the P2 specimen has influenced the enhancement of cathodic reactions, and is more dominant than the corresponding pre-strain effect. It should be noted that the pre-strain induced in case of the zone-2 specimens is also considerably low (Figure 1(a)). Therefore, dominant influence by the pre-strain in the form of facilitating cathodic reactions on fragmented cementite than damaged mill-scale has not been exhibited in the P2_with scale specimen. Hence, lower cathodic slopes in the P2 and P3 specimens (Table II) have been obtained when damaged scale was present on them. Instead, larger anodic activity has been facilitated on their surfaces, which can indeed be confirmed from the spontaneous passivity (Table II and Figures 3(b), (e)). In brief, local corrosion cell formation has greater influence than pre-strain on the polarization response of the zone-2 (P2 and P3) specimens.

On the other hand, the β_c values are higher in the zone-3 specimens (P4, P5 and P6) as compared to others (Table II). This confirms that there is a larger effect of oxygen reduction reaction in the zone-3 specimens than in other specimens. The fragmented cementite in zone-3 specimens due to higher pre-strain provides larger areas for cathodic activity,[47] and facilitates oxygen reduction. Moreover, there exists very little or no influence from the mill-scale in zone-3 specimens (Figure 1(c)). This denotes that the pre-strain in rebar has larger control on the corroding mechanism in zone-3 (P4, P5 and P6) specimens as compared to the zone-2 specimens (P2 and P3). Finally, it is the combined effect of mill-scale and strained microstructure (or cementite) on the polarization behavior.

Figure 4(a) shows the Nyquist plot of the specimens along with the magnified high-frequency data. The shapes of the depressed semicircles in the Nyquist plots clearly indicate the effect of the straining in the specimens. A careful observation of the high-frequency response (Figure 4(a)) clearly indicates the influence of mill-scale in the specimens P1, P2, and P3. The distinctive appearance of their recorded response near the real axis confirms the impact of high-frequency time constant. The high-frequency response of the zone-3 specimens, on the other hand, has not shown any signs of influence from high-frequency time constant indicating little or negligible influence of oxide scale. Thus, though the signature of passivity is not prominent in the polarization plot of the P1 (Figure 3(d)), its passive behavior has reflected in the high-frequency data during impedance analysis.

Figures 4(b) and (c) shows the Bode-magnitude and Bode-phase plots for the specimens. In all the specimens, the peak value of the Bode-phase has occurred in the low-frequency region (Figure 4(c)). While the peak of the phase in unstrained steel (P1) is not sharp (confirms the presence of more than one maximum), the peaks of strained specimens P2 and P3 are relatively sharper than that of P1 (Figure 4(c)). The peaks in P4, P5, and P6, on the other hand, have been observed to be very distinct and sharp, indicating only one time constant in the process (Figure 4(c)). This also signifies the gradual reduction in the influence of mill-scale at the rebar-metal interface due to its damaged condition.

Given the presence of mill-scale (Figure 1(c)) either in fully intact or partially damaged condition, the equivalent electric circuit-1 having two time constants as shown in Figure 4(d) has been used in the EIS analysis of P1, P2, and P3. Constant phase element (CPE) has been used to model the capacitance instead of pure capacitor, whose reactive term of the impedance is given by Eq. [4].

$$Z_{\mathrm{CPE}} = Q^{-1}(j\omega)^{-n} \qquad [4]$$

where Q is the admittance of the CPE, j is the imaginary unit representing the complex nature, n is the dispersion coefficient and ω is the angular frequency. Q_{ox} and Q_{dl} indicate the admittances of oxide layer and double layer, respectively. Accordingly, the equivalent circuit-1 can be represented as $R_s(Q_{\mathrm{ox}}(R_{\mathrm{ox}}(Q_{dl}R_{\mathrm{ct}})))$, in which the two time constants are $R_{\mathrm{ct}}Q_{dl}$ and $R_{\mathrm{ox}}Q_{\mathrm{ox}}$. While the low-frequency time constant $R_{\mathrm{ct}}Q_{dl}$ in Figure 4(d) corresponds to the double layer behavior, the high-frequency time constant $R_{\mathrm{ox}}Q_{\mathrm{ox}}$ is associated with the oxide scale. It is worth to mention that though the oxide scale is adhered to the metal substrate, it typically has pores and defects.[44,45] In the present study, the electrolyte is aggressive (3.5 pct NaCl solution), and therefore, the scale itself would not be stable in the electrolyte. In such cases, the transport of electrolyte from the scale's outer surface toward the metal–scale interface would occur easily through the connecting pores at a much rapid rate. Therefore, the capacitive reactance of the oxide layer, which is typically a delayed contribution to the effective resistance of the oxide layer, does not precede the double layer formation at the metal–electrolyte junction. Hence, the double layer formation has been assumed to happen in series with the resistance of oxide layer. Earlier works related to modeling the EIS data of carbon steels having mill-scale have also used similar circuit that has two time constants,[44,45] in which the RC loop of double layer was assumed to be within the RC loop of oxide layer. On the other hand, the EIS data of P4, P5 and P6 has been fitted using a simplified Randles circuit ($R_s(Q_{dl}R_{\mathrm{ct}})$) (equivalent circuit-2 shown in Figure 4(d)), as the specimens do not have significant influence of mill-scale (Figure 1(c)) and the passivity is also absent (Figure 3(f)). The EIS data have followed a very good fitting with both the circuits (χ^2 in the order of 10^{-3}), i.e., $R_s(Q_{\mathrm{ox}}(R_{\mathrm{ox}}(Q_{dl}R_{\mathrm{ct}})))$ and $R_s(Q_{dl}R_{\mathrm{ct}})$ in which R_s is the solution resistance, Q_{ox} and R_{ox} are the constant phase element (CPE) and resistance of the oxide layer on the steel, and, Q_{dl} and R_{ct} are the constant phase element (CPE) and charge-transfer resistance of the double layer. The fitted spectra are shown along with the measured spectra in Figures 4(a) through (c).
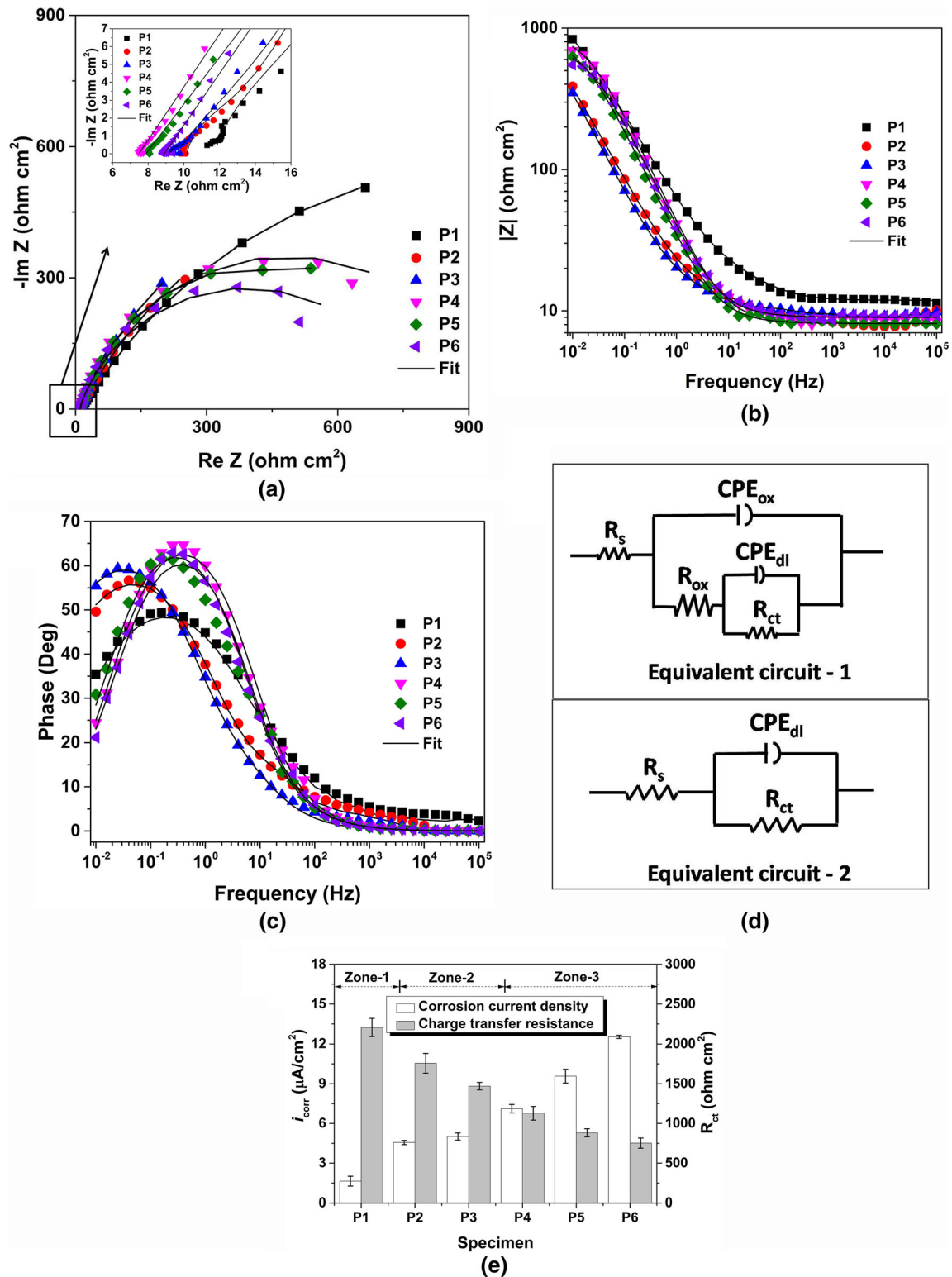
Fig. 4—(*a*) Nyquist, (*b*) Bode-magnitude, (*c*) Bode-phase plots of the specimens in 3.5 pct NaCl solution along with the fitted spectra. (*d*) Equivalent circuits-1 and 2 used to fit the spectra. (*e*) Comparative corrosion behavior of the specimens in 3.5 pct NaCl solution. (1) Different legends in Nyquist and Bode plots are the actual experimental data points and the black lines are the fitting results. (2) In (*e*), (i)$_{corr}$ values corresponding to P2 and P3 specimens are their passive current densities.

The quantitative information of the electrochemical parameters obtained from the data-fitting analysis is given in Table III. Since the dispersion coefficients are in the range of 0–1 (Table III), it can be inferred that all the specimens have exhibited mixed behavior between ideal resistor and capacitor. The values of R_{ox} in the P1, P2

Table III. Different Electrochemical Parameters Obtained After Fitting the Relevant Equivalent Circuits to the EIS Data of the Steels in the 3.5 pct NaCl Solution (Error Pct) is Mentioned in the Parenthesis

Specimen	R_s (Ω cm^2)	Q_{ox} (Ω^{-1}s^n cm^{-2}) (x 10^{-4})	n_{ox}	R_{ox} (Ω cm^2)	Q_{dl} (Ω^{-1}s^n cm^{-2}) (x 10^{-4})	n_{dl}	R_{ct} (Ω cm^2)
P1	11.72	12.91	0.81	10.64	42.25	0.62	2205
	(4.8)	(6.8)	(0.5)	(7.3)	(9.8)	(4.8)	(5.2)
P2	8.99	26.01	0.88	9.78	147.10	0.68	1757
	(4.2)	(9.2)	(0.1)	(1.1)	(6.3)	(3.2)	(7.1)
P3	9.92	78.74	0.95	5.75	179.93	0.77	1410
	(3.5)	(13.1)	(0.1)	(8.1)	(10.2)	(13.2)	(3.2)
P4	7.84	NA	NA	NA	69.19	0.74	1128
	(2.7)				(4.1)	(2.4)	(7.7)
P5	8.73	NA	NA	NA	62.72	0.79	882
	(2.4)				(3.7)	(2.0)	(5.7)
P6	9.00	NA	NA	NA	66.94	0.78	750
	(2.2)				(3.7)	(2.0)	(8.6)

For P1, P2 and P3, $R_s(Q_{ox}(R_{ox}(Q_{dl}R_{ct})))$, and for P4, P5 and P5, R$_s$(Q$_{dl}$R$_{ct}$)were fitted; NA: Not applicable.

and P3 (Table III) have reduced, indicating the damage occurred to the mill-scale on account of pre-straining. This effect has also been reflected in the form of a simultaneous increase in the admittance (Q_{ox}) of the oxide layer in them (Table III). The admittance of the double layer (Q_{dl}) formed at the interface has also increased in the order of P1, P2 and P3. This denotes the increased tendency of the active sites in P2 and P3 to exchange ions with the bulk electrolyte as compared to that in P1.

In general, the Q_{dl} values of the strained specimens that do not have mill-scale (P4, P5 and P6) have been observed to be higher than that of the unstrained steel (P1) (Table III), suggesting the higher number of active sites in the former than the latter, and also the greater tendency of the strained steels to exchange ions with the bulk electrolyte. However, the Q_{dl} values of the specimens P4, P5 and P6 (zone-3) are lower than that of zone-2 (P2 and P3) (Table III). This could be understood as a manifestation of the damaged mill-scale in P2 and P3. The presence of mill-scale in damaged condition would influence the active sites in P2 and P3, and resulted in exhibiting more tendencies to exchange ions. This increase in the capacitance behavior of the specimens P2 and P3 as compared to other specimens, has also reflected in the form of leftward shift of characteristic frequency (frequency corresponding to maximum phase angle) in the Bode-phase plot (Figure 4(c)).

The charge-transfer resistance of the specimen is dependent on the number of active sites present on the surface, and indicates the inherent tendency of a given active site to corrode. A comparative assessment on the effect of pre-induced plastic strains on the i_{corr} and the R_{ct} is shown in Figure 4(e). A steady increase in the i_{corr} and the corresponding decrease in the R_{ct} can be seen. The corrosion tendency of the rebars, which is a kinetic property, primarily depends on the nature of the reactions occurring on the electrode surface, and hence, influenced by its condition.[48] The damage to the mill-scale on account of introduction of plastic strains renders the underlying steel more susceptible to

corrosion. Moreover, the extent of galvanic coupling between the cementite and ferrite, in which cementite acts as cathode and ferrite acts as anode, is also an important factor that influences the corrosion rate.[47] The fragmented cementite due to higher levels of pre-tensioning (Figures 2(b) through (g)) would result in higher cathodic activity. This has been confirmed from the shift of cathodic branches in the polarization curves of the strained specimens. While the effect is directly noticeable in the zone-3 (P4, P5 and P6) specimens (Figure 3(f)) due to the little or no influence of mill-scale, the impact in zone-2 specimens has been noticed only when the damaged mill-scale is not present (Figure 3(c)). A simple corollary in the context of galvanic coupling in the microstructure helps in understanding the increased metal dissolution due to fragmentation of cementite. In the strained specimens, effectively more cementite portions are exposed to the electrolyte due to the fragmentation and kinking (Figures 2(c) through (g)). Cementite is relatively nobler than the ferrite in typical ferritic-pearlitic steel,[47] and hence, more cathodic portions would be exposed to electrolyte. Accordingly, the number of cathodic reactions increases in the strained specimens, which need electrons. These electrons have to come from the anodic site. Therefore, neighboring ferrite (Fe-phase), which is relatively anodic in nature, has to supply the electrons to the cathodic cementite. Thus, in brief, the increased cathodic activity due to fragmentation/bending of lamellae demands higher metal dissolution, and hence higher corrosion tendency has been observed in the strained specimens. Thus, the present results comply with the mechanochemical theory proposed by Gutman.[19]

On the other hand, the increase in the dislocation density upon pre-tensioning can be mainly attributed to the Lüders band formation in specimens with intermediate plastic strains for the zone-2,[49,50] and the dislocation pile-ups at the grain boundaries in the specimens with higher plastic strains for the zone-3.[51–53] It is well understood that the pinning of dislocations near the
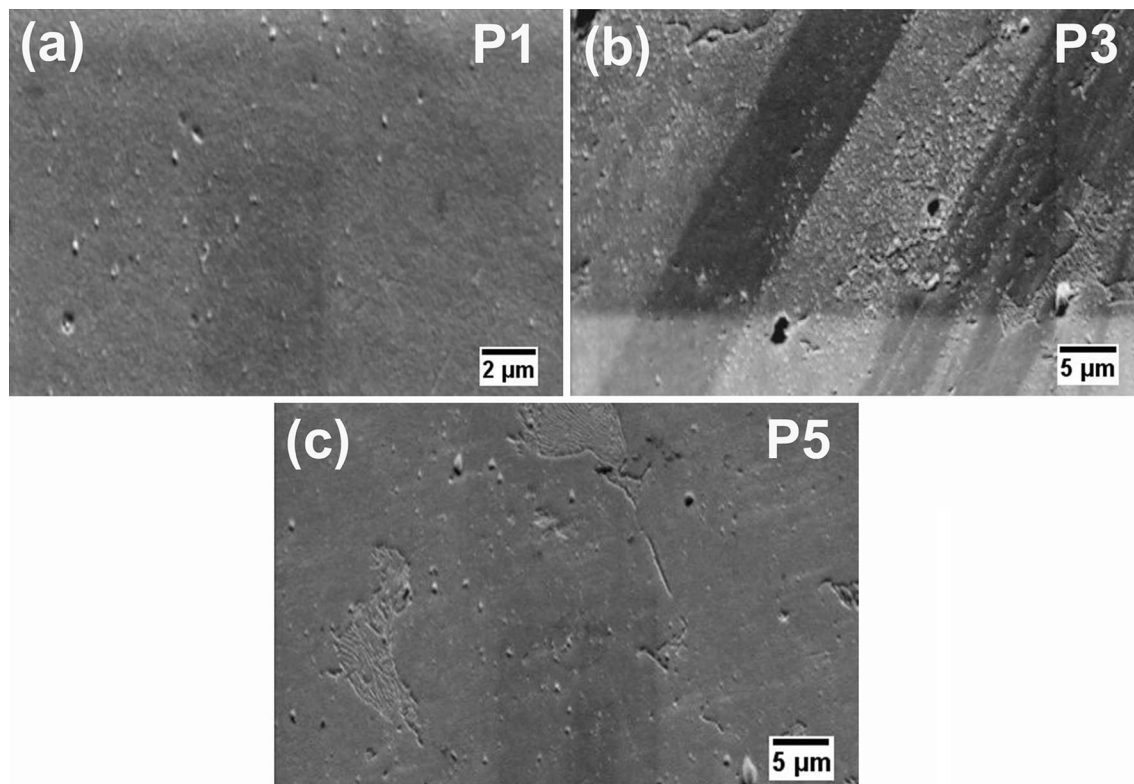
Fig. 5—High-resolution FE-SEM images obtained without etching the surface of polished (*a*) P1, (*b*) P3 and (*c*) P5 specimens. Distinctive surface appearance of the P3 specimen (Lüders band) can be seen.

vicinity of interstitial carbon atoms (point defects) in mild steel results in the locking of lattice strains in the Cottrell atmosphere, and therefore, tensioning the rebar beyond its yield limit would result in the local freeing of the point defects in the grains,[49,50] contributing to the release the strain energy accumulated due to such point defect interactions. However, due to creation of new dislocations, which has reflected in the form of slip lines (Lüders bands) in the specimens pertaining to zone-2, the energy of the system increases.[51] Thus, the increase in dislocation density occurs simultaneously with the Cottrell relaxation in zone-2, and at higher levels of pre-strain (in zone-2), the relaxation in Cottrell atmosphere becomes insignificant as compared to the increase in dislocations.[51,54] Accordingly, there will be a net increase in the free energy leading to the thermodynamic instability. In the present study, this effect has been reflected in the specimens with intermediate plastic strains (zone-2).

It has been understood that the inflection region between the end of yield plateau and start of the strain-hardening zone (*i.e.*, P3) is not only characterized with fully annihilated Cottrell atmospheres but also with the formation of Lüders bands, and this effect alters the surface finish due to the presence of stretch marks on the specimens, resulting in significant structural variation.[49,50] The variation of the exposed surface in the P3 as compared to other strained specimens can be clearly comprehended from Figure 5, which shows the FE-SEM images of some polished specimens that have been obtained without etching. The Lüders band formation is clearly visible in Figure 5(b). This could also attribute to the passivity in the polarization plot in case of the P2 and P3 (Figure 3(e)) as explained in the subsequent paragraph. At high levels of pre-induced plastic strain, the dislocation density near the grain boundaries increases,[49–54] and thus, results in significant thermodynamic instability in the specimens pertaining to zone-3. This can be better comprehended by reiterating the fundamental understanding on the response of carbon steel when subjected to uni-axial tension load.[49,50] Under an applied uni-axial tensile stress, the already existing dislocations and the new dislocations generated by Frank-Read sources move through the crystal lattice until they encounter a grain boundary. These boundaries act as impeding borders to the dislocation movement, and thus prevent the dislocation propagation. As the stress levels increase, more dislocations reach the boundary, leading to the formation of dislocation pile-up. Thus, the strain energy imparted to the rebar through uni-axial tensioning is stored in the form of piled-up energy near the grain boundaries, and ultimately cause the instability in the specimens.[40,50]

The Lüders band formed in the form of stretch marks in zone-2 specimens (Figure 5(b)) leads to the variation in their surface locally. Thus, the passivity phenomenon in the polarization scan of the specimens belonging to

the zone-2 (Figure 3(e)), which is primarily due to presence of partially damaged mill-scale, could be influenced by the formation of stretch marks (Lüders band) on the surface. On the other hand, in the zone-3 specimens, dislocations accumulate near the grain boundaries (known as dislocation pile-up),[51,52] and the specimens are not characterized with any stretch marks on the surface due to the increase in the dislocation density as shown in Figure 5(c). Further, mill-scale is absent in zone-3 specimens, and thus, there is no surface covering effect in them. Hence, the specimens pertaining to zone-3 have not exhibited passivity during the potentiodynamic polarization scan (Figure 3(f)).

C. Corrosion of the Strained Rebars Under Salt-Fog Tests

In general, the rebar specimens having pre-induced plastic strains have shown higher i_{corr} and lower R_{ct} than the unstrained specimens in the Phase-I (Figure 4(e)). To understand the corrosion behavior of the strained steels from the viewpoint of nature of the corrosion products formed, studies have been carried out using the specimens of the unstrained and pre-strained rebars. The specimens, P1, P3 and P5, have been chosen for the purpose, since P3 and P5 represented specimens with intermediate and high levels of plastic strain and P1 is the as-received specimen.

Typical FTIR spectra of the rust samples collected from the specimens subjected to different exposure duration in salt-fog are shown in Figures 6(a) through (d), and the FE-SEM micrographs of some selected rusted surfaces are shown in Figures 7(a) through (f). Existence of a phase in a given rust sample has been confirmed by observing the dips in the FTIR spectrum at the respective characteristic wavenumbers.[55] Table IV summarizes the corrosion products found in the rust samples along with their transmittance values (pct). Strong and sharper dips at the wave numbers of 480, 620 and 1020 cm^{-1} in FTIR spectrum correspond to Fe(OH)$_2$, γ-Fe$_2$O$_3$ and γ-FeOOH, respectively.[55] The relatively broader dips in the range of 630–700 cm^{-1} and 800–900 cm^{-1} in the spectra indicate the presence of β-FeOOH and α-FeOOH, respectively.[55] From Figures 6(a) through (d), it is clearly evident that the observed wavenumbers are noticeably closer to their characteristic values.

Figures 8 and 9 show the evolution of the OCP with time and the over-potentials as a function of the current densities in freely aerated 3.5 pct NaCl solution in the rusted steel specimens (P1, P3 and P5) after exposing to different time-periods in the salt-fog chamber, respectively. The stabilized OCP values and the corresponding R_P values obtained using the procedure described in Section IIB(2) are summarized in Table V. In general, the rust formed on the strained rebars (P3 and P5) shows nobler behavior (relatively positive OCP) compared to the control unstrained rebar (P1). Particularly, the OCP of the rusts formed on P3 has been observed to be nobler than the remaining.

1. Variation in the compositions of the rusts as a function of time

Cyclic wetting and drying of the steel specimens inside the fog chamber has promoted continuous dissolution followed by hydrolysis of iron throughout the test period.[56] Indeed, this effect is reflected in the form of predominant dips of Fe(OH)$_2$ in all the samples (Figures 6(a) through (d)). However, for a given steel, the intensities of the dips of Fe(OH)$_2$ have increased till Day-20 followed by a subsequent drop. γ-FeOOH and α-FeOOH have been identified in all the samples, whereas β-FeOOH has been observed only in the samples collected on Day-5 and Day-10. Conformingly, flowery structure of γ-FeOOH[30] and sharp crystalline form of α-FeOOH[33] have been observed in the SEM micrographs of the rusted surfaces (Figures 7(a) and (b)). Particularly, it can be observed from Figures 6(a), (b) that there is an increase in the transmittance values of β-FeOOH from Day-5 to Day-10 in all the steels, and this confirms its gradual transformation into other oxy-hydroxide or oxide form. It should be borne in mind that the direct interaction of chloride ions with Fe is required for the formation of β-FeOOH.[24] After the surface is fully covered with corrosion products (in between Day-5 to Day-10), there exists very limited possibility for the chloride ions to attack fresh metal surface. This could also contribute to the absence of β-FeOOH in the rust samples collected after Day-10.

On the other hand, γ-Fe$_2$O$_3$, a stable oxide form of iron, has not been observed in any of the samples collected on Day-5 and Day-10. However, its presence in all the samples collected on Day-20 and Day-30 has been noticed. Thus, the presence of the oxide phases in the rusts and the corresponding decrease in the oxy-hydroxides in Day-20 and Day-30 rust samples have confirmed the gradual stabilization of rust with time. In other words, the initially formed γ-FeOOH in all the steels could have transformed either into stable α-FeOOH or γ-Fe$_2$O$_3$ with time. Significant presence of crystalline and whisker forms of α-FeOOH,[32] and sandy-grain structure of γ-Fe$_2$O$_3$[32] can be clearly seen in Day-20 and Day-30 rusted surfaces (Figures 7(c) through (f)).

Indeed, the transformation of γ-FeOOH that forms on the metal surface in neutral solutions into other stable forms of rust has been reported in the literature.[56–60] However, the above transformation depends largely on the feasibility for oxidation and dehydration processes to occur in the corroding system.[56] It should be noted that in the present study, the corrosion tests have been performed in a controlled environment (salt-fog chamber), and therefore, the variations in the relative presence of different phases can be solely attributed to the tendency of the rebar surface to support the transformation process, which is different for different specimens due to the presence of different amounts of plastic strain.

The temporal variations in the relative proportions of phases can be better interpreted using the $\alpha/\gamma*$ ratio of the rust. Previous researches on the mechanism of formation of corrosion products and their subsequent stabilization have reported the $\alpha/\gamma*$ of rusts, indicating
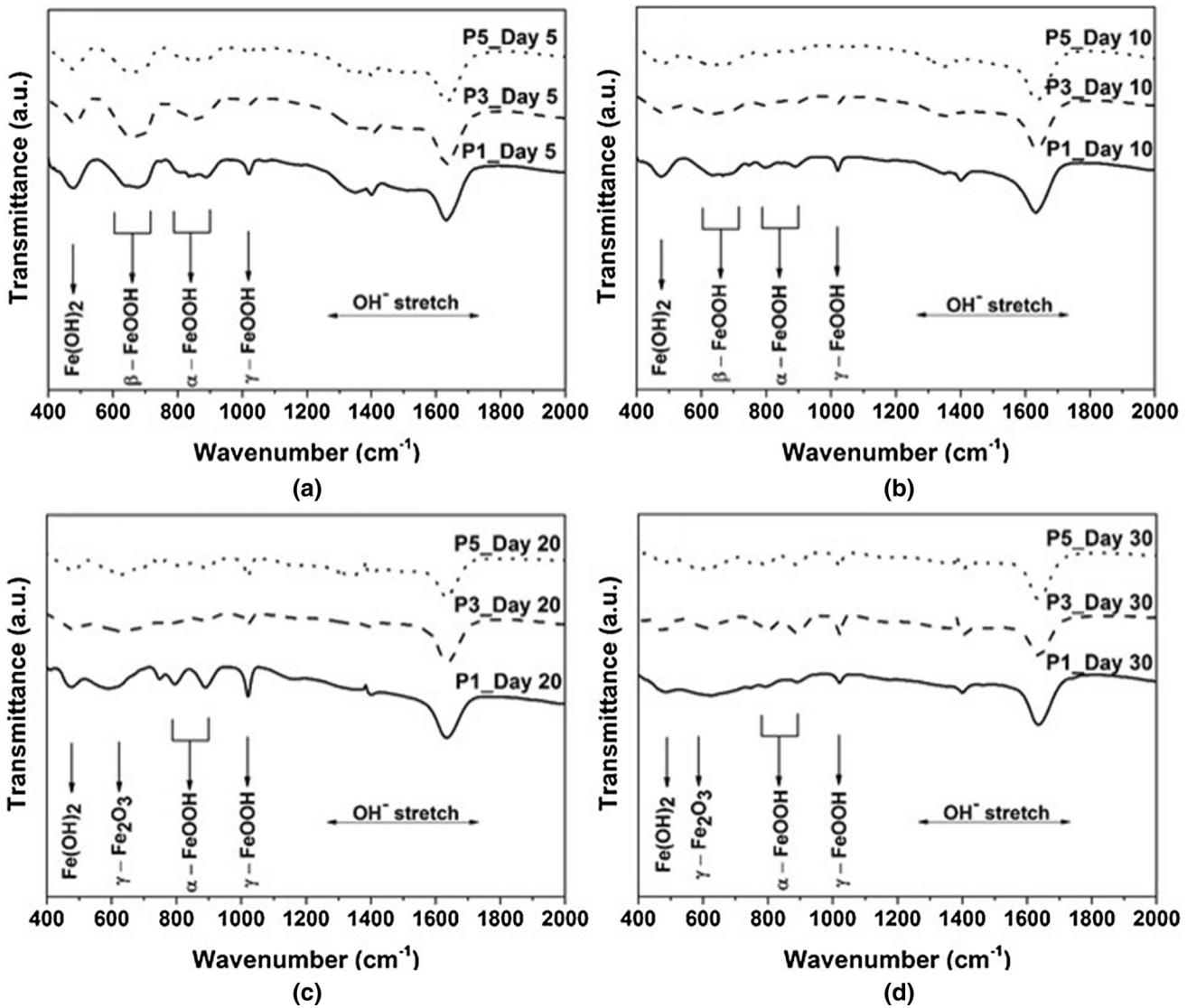
Fig. 6—FTIR spectra of rust samples collected from different specimens (P1, P3 and P5) after (*a*) 5 days, (*b*) 10 days, (*c*) 20 days and (*d*) 30 days of salt-fog exposure.

the protectiveness of the rust adhered on the specimens.[32–35] Values of α/γ* ratio are calculated based on the quantitative fractions (determined using the procedure described in Section IIB(2)) and given in Table V.

A comparative assessment of the change in α/γ* of rusts formed on the different strained steels pertaining to their respective exposure periods is shown in Figures 10(a) through (c), from which it can be clearly inferred that there is a decrease in α/γ* ratio of the rusts from Day-5 to Day-10 in all the samples. This effect has pronounced in all the steels irrespective of the amount of plastic strain present in them. The initial reduction of α/γ* can be attributed to the formation of unstable rust on the specimens, as the phases are nascent at Day-10. Choudhary *et al.*[32] have also reported an initial reduction of α/γ* of rusts formed on mild steels. Furthermore, it has been clearly established in the literature that the corrosion on the rebar starts as a localized attack at specific sites during the initial stages,

and gradually evolves as uniform corrosion on its surface.[32] Conformingly, in this study, localized rust formation at selective sites on the surfaces has been noticed in the Day-5 specimens, which can be clearly comprehended from Figure 7(a).

The freshly formed rusts during the initial stages consist of porous constituents, like γ-FeOOH and β-FeOOH, in substantial amounts (Table IV), and therefore, a strong possibility for the differential concentrations of oxygen and chlorides on the same surface of the specimens would exist. Thus, the rust formed initially at selective locations promotes a galvanic action between the freshly exposed metal portion and the locations having rust.[32] In a nut-shell, along with the chloride ions available in the chamber, the galvanic action has facilitated further corrosion on the surface. Interestingly, α/γ* values are nearly same for all the steels at this stage (Day-10). The extensive formation of rust, yet not in the stabilized state, would probably have
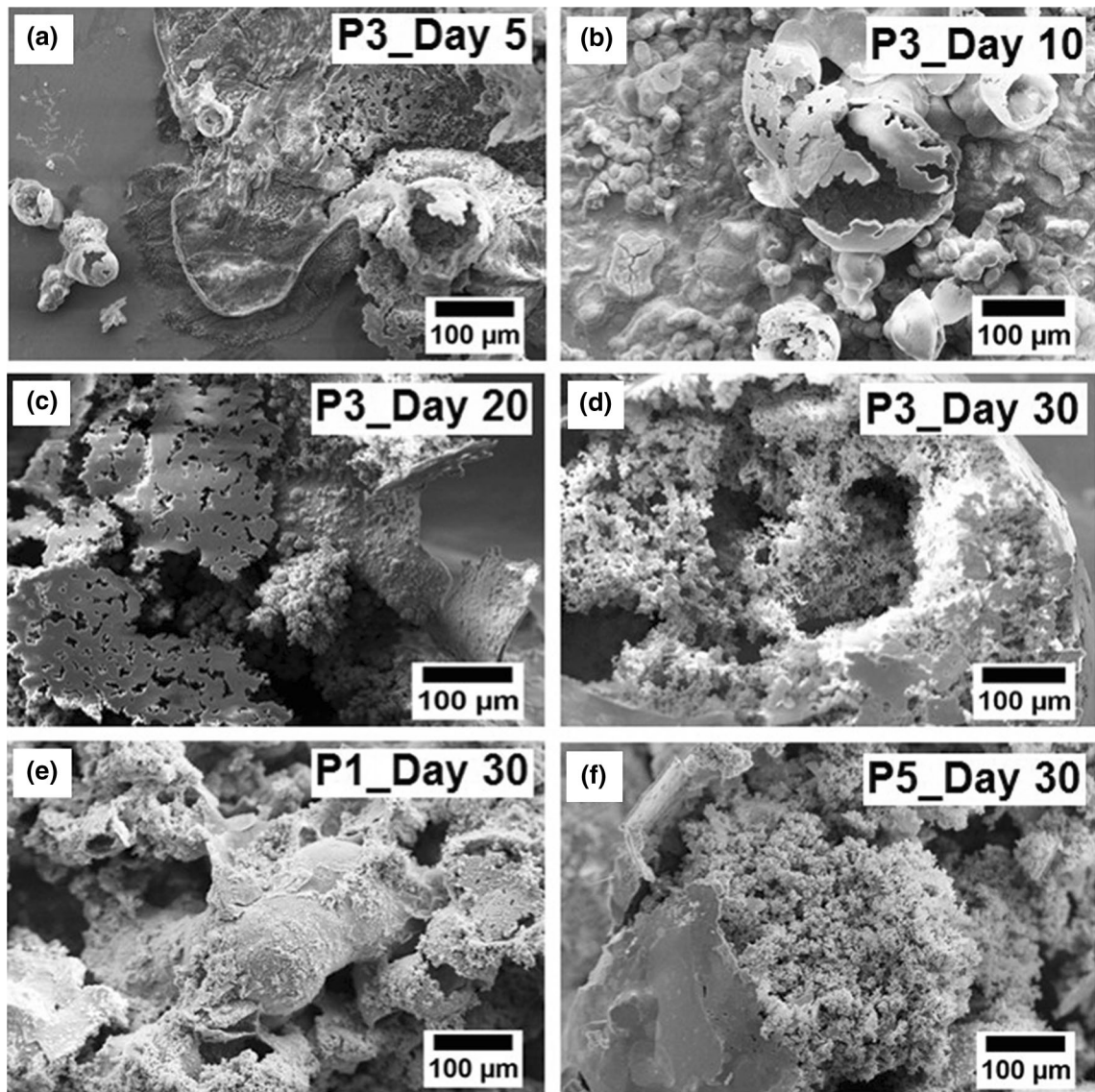
Fig. 7—FE-SEM images of the rusted P3 specimens obtained after (*a*) 5 days, (*b*) 10 days, (*c*) 20 days and (*d*) 30 days of salt-fog exposure. SEM micrographs of the rusted surfaces of (*e*) P1 and (*f*) P5 after 30 days of exposure. These are representative observations.

kept the effect of pre-tensioning out of sight on Day-10. A steady increase in the protective ability (α/γ^*) of rusts can be observed in all the steels from Day-10 to Day-30 (Figures 10(a) through (c)), which is a result of gradual transformation of unstable corrosion products into stable form.

2. *Variation in the electrochemical behavior of rusted steel specimens as a function of time*

Comparative OCP behavior and the R_P of various rusted specimens are shown in Figures 10(a) through (c). Irrespective of the extent of pre-tensioning, OCP, indicating the thermodynamic stability of the rusts formed on different specimens, has shifted to more positive values (Figures 10(a) through (c)). This indicates the gradual reduction in the tendency of the rusted metal surface to exchange the ions with the bulk electrolyte due to the stabilization of the rust. The

potential would adjust itself depending on the formation of different rust phases (soluble and protective) as well as the thickness of the rust layer formed during the salt-fog exposure. However, at this moment, it is not clear which one would influence more on the change in OCP. Hence, data in Figure 10 are the result of combined effect from the thickness and rust phases on the potential and R_P values.

The R_P values of the specimens show a reduction at the Day-10 exposure level (with respect to Day-5 level), and a steady increase after that, as reported in the literature.[32] This behavior can be attributed to the tendency for the galvanic coupling between the electrochemically dissimilar phases, such as cementite lamellae and ferrite in pearlitic colonies playing crucial role in the initial stages. Moreover, it has been discussed earlier that the specimen exposed for 5 days shows localized attack with rust formation at some location, leaving

other regions relatively rust-free (Figure 7(a)). This creates a galvanic couple between rusted portion, which acts as cathode, and exposed region acting as anode. The specimens at the end of Day-10 are characterized with uniform rust formation on their surface, and it is interesting to note that the R_P values of the Day-10 specimens for all the steels tested are nearly equal. This would have manifested in the form of a reduction of the polarization resistance at Day-10 as compared to Day-5. This is also in line with the observation made by Choudhary et al.[32]

Beyond the Day-10 period, once the specimen is covered with rust, further electrochemical behavior would expectedly depend on the rust layer formed on the specimens. This rust layer tends to 'protect' the metal surface causing an increase in the R_P and the OCP value shifting to nobler levels, after the Day-10 exposure (Table V). The increase in the R_P values is also corroborated by the considerable amounts of oxide forms of rust (γ-Fe_2O_3) in Day-20 and Day-30 samples, which are relatively less porous than the oxy-hydroxide forms. Substantial amounts of oxy-hydroxide forms have been noticed in the rust samples of Day-5 and Day-10 specimens (Figures 6(a) through (d) and Table IV). It can, thus, be stated that the stabilization of the corrosion products plays an instrumental role in obtaining higher R_P values in Day-20 and Day-30 samples, due to longer exposure period.

The variation in the corrosion tendencies of the rusted steels over time as discussed above, confirm that their interaction with the neighboring environment depends on the nature of the corrosion products formed on the steel surface.[59,60] In fact, a strong correlation between the protection afforded by the corrosion products as measured by the α/γ^* ratio, the OCP and the polarization resistances (R_P) has been observed in the study (Figures 10(a) through (c)). It can be seen that in all the cases, the initial decrease in α/γ^* from Day-5 to Day-10 has been accompanied with an increase in the OCP and a corresponding decrease in the R_P. It should be borne in mind that relatively non-protective rust would allow more oxygen and moisture to reach the metal surface, and promote further corrosion. Thus, the gradual stabilization of corrosion products during the later stages (Day-10 to Day-30) has not only been characterized by obtaining higher protectiveness of the rust (α/γ^*) but also by the accompanying steady increase in the polarization resistance of the rusted steel (Table V).

3. Effect of plastic strains on the nature of the rust

The effect of plastic strains on the electrochemical properties of the rusted steels can be comprehended from Figures 10(d) through (f). It can be seen from Figure 10(d) that the R_P of Day-5 specimens decreases in the order of moderately strained—heavily strained—unstrained. Moreover, considerable differences in the composition of the rusts formed on various strained specimens at the end of Day-5 have also been noticed (Table IV). Both the R_P values of the Day-10 corroded-strained specimens and the protective abilities of their rusts have been obtained to be nearly equal. However, the α/γ^* of the rusts and R_P values of the corroded specimens at the end of Day-20 and Day-30 have again observed to decrease in the order of: moderately strained—heavily strained—unstrained (Figures 10(e), (f)).

In general, the results from the salt-fog tests have shown that irrespective of the exposure period, the rusts formed on the strained specimens have higher protective abilities (α/γ^*) and lead to a recording of higher polarization resistances (R_P) of the specimen. This behavior could be due to their high initial corrosion rates, which would have led to more rust formation that eventually results in higher proportion of stabilized rust on the surface of the strained specimen.

The protective ability (α/γ^*) of the rusts formed on the moderately strained specimen (P3) have been observed to be higher than that of heavily strained specimens in all the cases (Table V). The rusted specimens with moderate levels of pre-induced plastic strains have always shown higher polarization resistances than the specimens of heavily strained and unstrained steels. Thus, results in Phase-II clearly show that the corrosion products formed on the P3 specimens are more stable, which has reflected in the form of passivity in Figure 3(e).

In brief, the results of the protective behavior of the rusts obtained in Phase-II are the manifestation of relatively higher initial corrosion rates in the strained steels, and thus, they are in coherence with their polarization behavior (R_P and i_{corr}) in Phase-I. The peculiar behavior of the P3 has been ascribed to the feasibility for the galvanic process to occur on its surface due to the partial damage occurred to the mill-scale and also to the Lüders band formation. However, higher corrosion rates on the account of plastic strains are mainly due to the damage to the cementite lamella that has led to the increase in the metal dissolution rate. Ennoblement of the rebar at high levels of plastic strain has been attributed to the complete removal of mill-scale, which has eventually reduced the galvanic effect between the scaled and un-scaled portion. In addition, the investigation carried out on the nature of the rusts formed on the moderately strained steels in Phase-II has shown their inherent tendency to form stable corrosion products, and thus, confirmed their passivation behavior.

In general, it is clear that the pre-induced plastic strains in the rebar result in significant formation of rust on its surface. Even in the absence of pre-strain, the surface of the rebar is usually covered with an oxide scale (i.e., mill-scale), and could be covered with corrosion products on the surface in harsh environment. When such rebars are put in the formwork before concreting, the passivation phenomenon can be expected to be affected as the bare metal does not get exposed to high pH concrete environment. This is primarily because the formation of passive layer on the rebar in concrete, which is semi-conducting in nature, is largely influenced by its surface condition.[61,62]

The nature of the corrosion products present on the rebar surface also influences the passive layer formation, as they have varying electrochemical characteristics. For instance, steel sample (bare metal) has been

Table IV. Values of FTIR Transmittance Peak Intensities of Different Phases Present in the Rust Samples

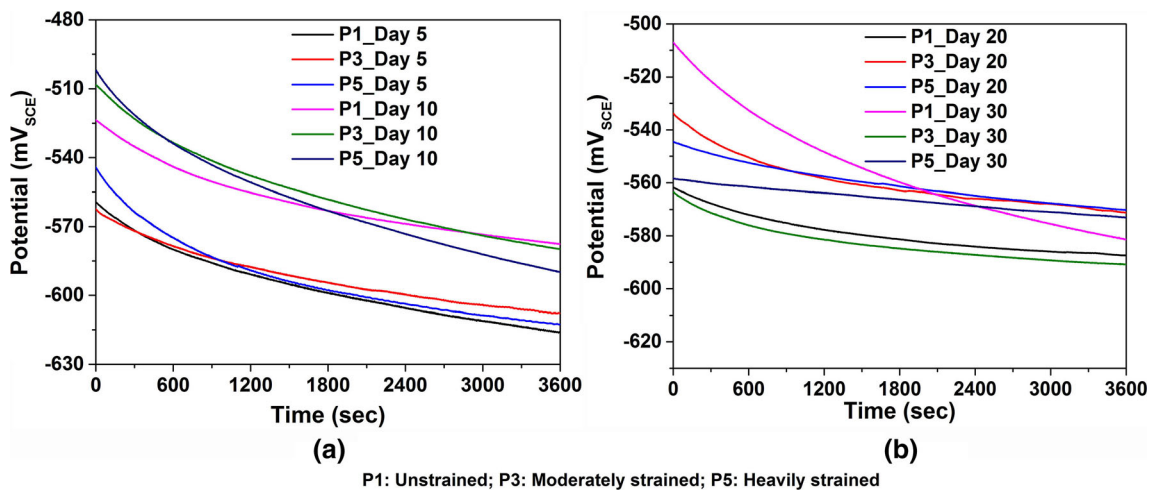| Rebars	Duration	γ – FeOOH (1020 cm^{-1})	α – FeOOH (800-900 cm^{-1})	β – FeOOH (630-700 cm^{-1})	γ – Fe$_2$O$_3$ (620 cm^{-1})	Fe(OH)$_2$ (480 cm^{-1})
			Rust Phases [55] and Transmittance Values (Pct)			
Unstrained (P1)	Day 5	86.0	85.0	74.0	⊗	73.0
	Day 10	87.0	91.0	82.7	⊗	82.1
	Day 20	73.6	92.0	⊗	80.0	82.0
	Day 30	91.0	82.0	⊗	80.0	83.0
Moderately strained (P3)	Day 5	94.0	80.0	66.0	⊗	77.0
	Day 10	93.0	93.0	83.0	⊗	85.0
	Day 20	91.0	93.0	⊗	85.0	86.5
	Day 30	82.0	82.8	⊗	87.8	85.3
Heavily strained (P5)	Day 5	94.0	88.0	77.0	⊗	80.0
	Day 10	96.0	94.0	82.0	⊗	83.0
	Day 20	78.0	86.0	⊗	80.0	94.0
	Day 30	87.0	88.0	⊗	85.0	91.0

⊗Presence has not been found.

P1: Unstrained; P3: Moderately strained; P5: Heavily strained

Fig. 8—Variation of OCP with time for the rusted specimens in 3.5 pct NaCl solution taken (*a*) after 5 and 10 days, and (*b*) after 20 and 30 days of salt-fog exposure..

reported to be least noble in potential followed by Magnetite (Fe$_3$O$_4$) and Hematite (Fe$_2$O$_3$) in both chloride-free and chloride-contaminated Ca(OH)$_2$ solution.[63,64] The anodic currents for Hematite and Magnetite samples have also been reported to be lower than that of Wustite (FeO) in chloride-free pore solution.[63] The existence of oxy-hydroxide component in the corrosion product could effectively increase the anodic currents on oxidized steel samples.[63] Thus, the passive currents are influenced not only by the presence of oxides on rebar but also by their composition. Furthermore, it is rational to conclude that the amount of corrosion products could also be as influential as their nature, as far as the formation of passive layer is concerned. However, it is very difficult to segregate the effect of such phenomena. So, the analysis carried out in the present study is based on the formation of different rust phases, considering the fact that the dissolving rust phases or formation of protective rust phases would finally come in contact with the corrosive ions in the electrolyte. However, the discontinuous

presence of corrosion products on the rebar could also be influential in the passivation phenomenon. The possibility for the formation of local corrosion cells if the corroded bar gets into contact with bare rebar in concrete cannot be ignored. The oxidized portions could support the cathodic reactions due to their higher nobility as compared to bare metal, and therefore, larger the extent of pre-oxidation, more would be the risk for bare metal.

The passive layer formation in concrete is plausibly more related to the stable nature of the corrosion products formed on the surface of rebar. Since the oxides formed on the strained specimens of P2–P6 (zones-2 and 3) have shown higher protectiveness than unstrained (P1) specimens (zone-1) (Table V), the surface conditions in corroded P1 specimen would facilitate better passive layer formation as compared to the strained specimens. However, the influence of pre-existing mill-scale, whether it is fully covered or partially damaged (due to straining) could definitely
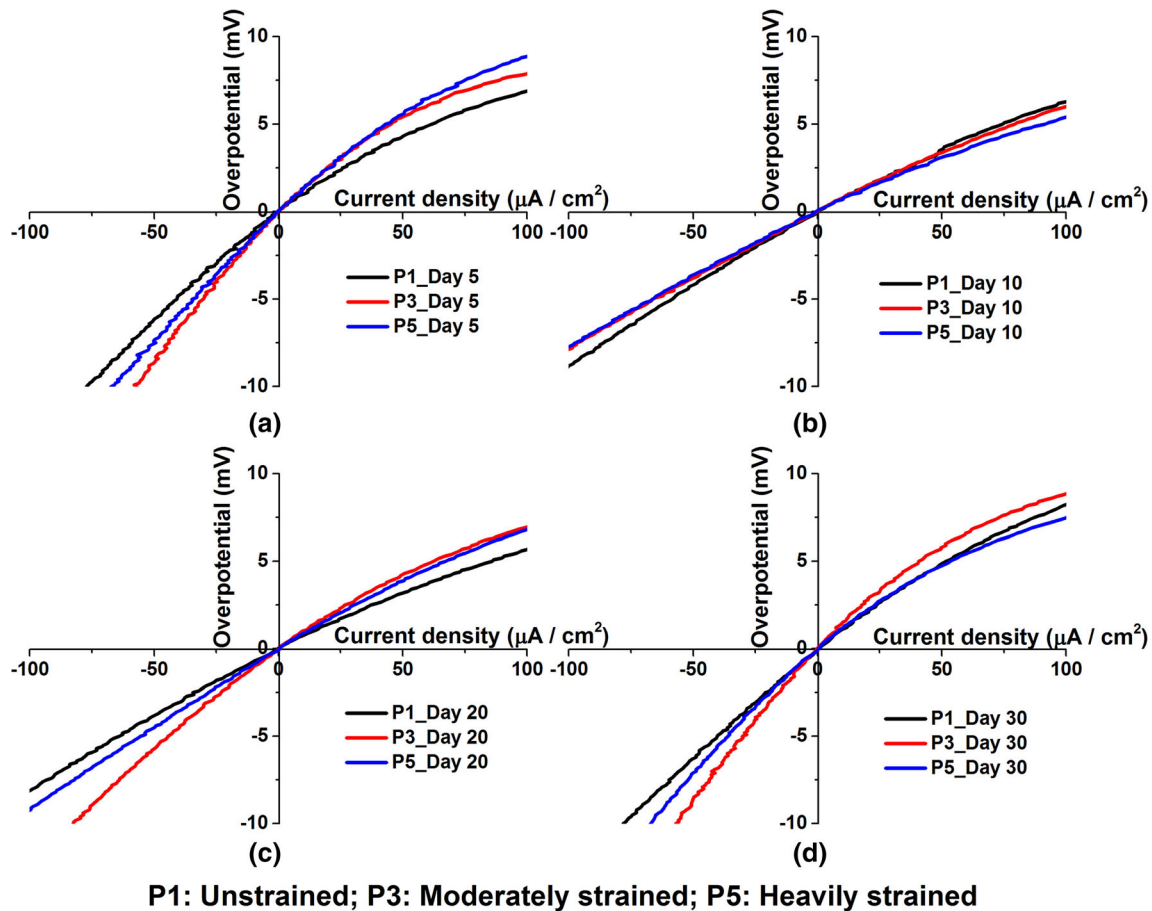
P1: Unstrained; P3: Moderately strained; P5: Heavily strained

Fig. 9—Linear polarization measurements of the already corroded specimens in 3.5 pct NaCl solution after (*a*) 5 days, (*b*) 10 days, (*c*) 20 days and (*d*) 30 days of salt-fog exposure.

have influence when they are embedded in concrete, and this can be subject of serious analysis in future.

Similar phenomenon of increased corrosion activity of X100 pipeline steels in bicarbonate solution due to plastic strains has been reported by Xu *et al.*[53] However, a closer examination has revealed that the X100 steel used in the aforementioned study does not contain any yield plateau region, and neither the effect of scale has been considered by the authors.[53] Moreover, the slight increase in the corrosion resistance near the junction of yield and strain-hardening regions has been ignored.[53] The present results exclusively depict the corrosion behavior of rebars, which are generally subjected to enormous amounts of pre-induced plastic strains at bends and hooks in reinforced concrete (RC) structures.

IV. CONCLUSIONS

Electrochemical measurements carried out on the rebar specimens in 3.5 pct NaCl solution have shown that pre-induced plastic strains tend to decrease their corrosion resistance. The increase in the corrosion tendencies of the strained rebars is mainly due to the

changes in the surface condition arising on the account of the damage to the mill-scale and also to the changes occurred to the cementite lamellae, which has resulted in more cathodic activity. Higher levels of pre-strain have resulted in severely bent, fractured and kinked cementite lamellae, which have led to the increased metal dissolution. In addition, the specimens strained till the easy-slip zone (zone-2) of the stress–strain curve have exhibited passivity due to the formation of local corrosion cells between scaled and un-scaled portions. On the other hand, the specimens pre-tensioned till the strain-hardening zone (zone-3) have not shown any passivity, and have been observed to experience larger impact from concentration polarization due to negligible influence from the mill-scale.

The corrosion potentials (E_{corr}) of the strained rebars are more negative than the unstrained ones. The Lüders band formation and the increase in dislocation density near the grain boundaries (grain boundary strengthening) are the contributing factors for the thermodynamic instability in the specimens pertaining to zones-2 and 3, respectively. However, ennoblement of the strained rebars at high levels of plastic strains has been noticed, and this is due to the reduction in the galvanic effect between the scaled and un-scaled portions in zone-3

Table V. α/γ^* Ratio and the Electrochemical Measurements of Rusted Rebar Specimens in 3.5 pct NaCl Solution Under Different Levels of Exposure

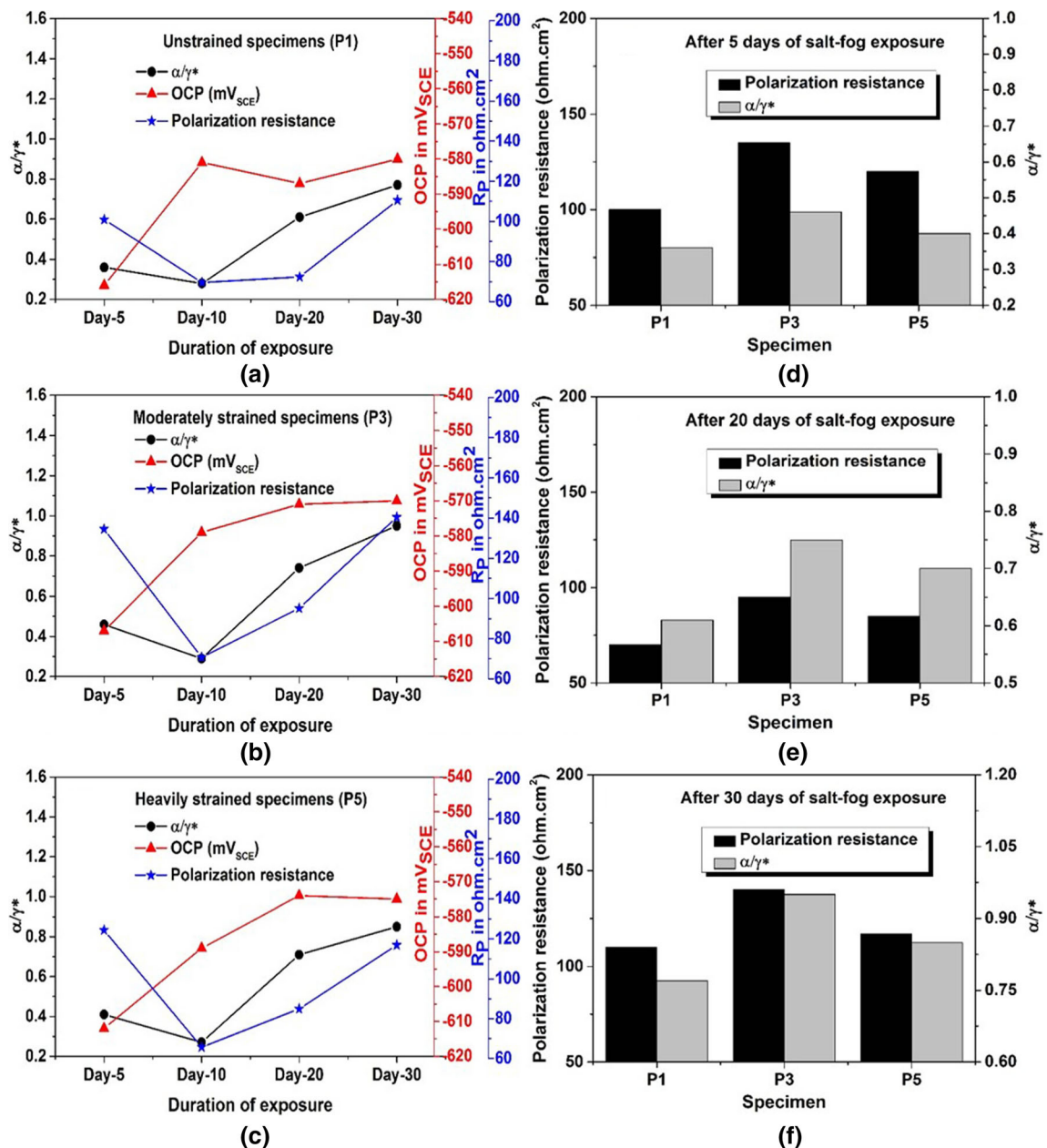| Exposure Time (days)	Unstrained (P1)			Moderately Strained (P3)			Heavily Strained (P5)		
	OCP (mV$_{SCE}$)	R_P ($\Omega.cm^2$)	α/γ^*	OCP (mV$_{SCE}$)	R_P ($\Omega.cm^2$)	α/γ^*	OCP (mV$_{SCE}$)	R_P ($\Omega.cm^2$)	α/γ^*
5	− 616	100.8	0.36	− 607	134.5	0.46	− 612	124.4	0.41
10	− 581	69.5	0.28	− 579	70.7	0.29	− 589	65.7	0.27
20	− 587	72.3	0.61	− 571	95.1	0.75	− 574	84.9	0.71
30	− 580	110.5	0.77	− 570	140.4	0.95	− 575	116.9	0.85

Fig. 10—Variation of the α/γ^* ratio, OCP and R$_P$ after different exposure durations for the rusted steels (a) P1, (b) P3 and (c) P5. Typical comparative behavior of various rusted steel specimens (having different levels of pre-induced plastic strains) after (d) 5, (e) 20 and (f) 30 days of salt-fog exposure.

specimens. Furthermore, the investigation carried out on the nature of the rusts formed on the various strained rebars has confirmed the formation of relatively stable corrosion products after certain period of time. The variation in the R_P values of the corroded-strained rebars has been observed to follow a very good correlation with the corresponding protective abilities (α/γ^*) of the rusts.

REFERENCES

1. L.A. Erasmus: *Concr. Int.*, 1981, vol. 3, pp. 47–52.
2. K. Babaei and N.M. Hawkins: *Concr. Int.*, 1992, vol. 14, pp. 67–72.
3. S.R. Humphreys and A.L. Felder: *Technical Note CTN-G-1-14*, CRSI, Schaumburg, Illinois, 2014, pp. 1–12.
4. ACI committee: Report No. 318R-14, ACI, Farmington Hills, MI, September 2014.
5. J.P. Broomfield: *Corrosion of steel in concrete – understanding, investigation and repair*, 2nd ed., Taylor & Francis, Oxon, 2007, pp. 6–10.
6. Z.P. Bažant: *J. Struct. Div.*, 1979, vol. 105, pp. 1137–53.
7. A.S. Al-Harthy, M.G. Stewart, and J. Mullard: *Mag. Concr. Res.*, 2011, vol. 63, pp. 655–67.
8. Y. Zhou, B. Gencturk, K. Willam, and A. Attar: *J. Mater. Civ. Eng.*, 2015, vol. 27, p. 04014245.
9. S. Yoon, K. Wang, W.J. Weiss, and S.P. Shah: *ACI Struct. J.*, 2000, vol. 97, pp. 637–44.
10. T. El Maaddawy, K. Soudki, and T. Topper: *ACI Struct. J.*, 2005, vol. 102, pp. 649–56.
11. G. Malumbela, M. Alexander, and P. Moyo: *Eng. Struct.*, 2009, vol. 31, pp. 2518–25.
12. A. Ababneh and M. Sheban: *Mater. Struct. Constr.*, 2011, vol. 44, pp. 1123–37.
13. Y. Du, M. Cullen, and C. Li: *Constr. Build. Mater.*, 2013, vol. 39, pp. 148–52.
14. J. Dong, Y. Zhao, K. Wang, and W. Jin: *Constr. Build. Mater.*, 2017, vol. 151, pp. 208–19.
15. C. Fu, N. Jin, H. Ye, X. Jin, and W. Dai: *Corros. Sci.*, 2017, vol. 117, pp. 11–23.
16. S. Zhang, X. Pang, Y. Wang, and K. Gao: *Corros. Sci.*, 2013, vol. 75, pp. 293–99.
17. X. Feng, X. Lu, Y. Zuo, N. Zhuang, and D. Chen: *Corros. Sci.*, 2016, vol. 103, pp. 66–74.
18. H. Li and X. Wu: *J. Mater. Civ. Eng.*, 2018, vol. 30, p. 04017311.
19. E.M. Gutman: *Mechanochemistry and corrosion prevention of METALS*, Science Publication in Chinese, Peking, 1989.
20. C.A. Apostolopoulos and D. Michalopoulos: *Mater. Corros.*, 2007, vol. 58, pp. 1–12.
21. Y. Zhang and A. Poursaee: *J. Mater. Civ. Eng.*, 2015, vol. 27, p. 04014234.
22. X. Feng, Y. Zuo, Y. Tang, X. Zhao, and X. Lu: *Electrochim. Acta.*, 2011, vol. 58, pp. 258–63.
23. X. Feng, Y. Tang, and Y. Zuo: *Corros. Sci.*, 2011, vol. 53, pp. 1304–11.
24. P.K. Behera, A.P.K. Moon, K. Mondal, and S. Misra: *J. Mater. Civ. Eng.*, 2016, vol. 28, p. 04016158.
25. B. Eghbali: *Mater. Lett.*, 2007, vol. 61, pp. 4006–10.
26. S. Torizuka, A. Ohmori, S.V.S.N. Murthy, and K. Nagai: *Scripta Mater.*, 2006, vol. 54, pp. 563–68.
27. S. Choudhary, V. Nanda, S. Shekar, A. Garg, and K. Mondal: *J. Mater. Eng. Perform.*, 2017, vol. 26, pp. 185–94.
28. K. Suda, S. Misra, and K. Motohashi: *Corros. Sci.*, 1993, vol. 35, pp. 1543–49.
29. S.J. Jaffer and C.M. Hansson: *Cem. Concr. Res.*, 2009, vol. 39, pp. 116–25.
30. T.D. Marcotte and C.M. Hansson: *Mater. Struct. Constr.*, 2007, vol. 40, pp. 325–40.
31. J.K. Singh and D.D.N. Singh: *Corros. Sci.*, 2012, vol. 56, pp. 129–42.
32. S. Choudhary, A. Garg, and K. Mondal: *J. Mater. Eng. Perform.*, 2016, vol. 25, pp. 2969–76.
33. P. Dillmann, F. Mazaudier, and S. Hœrlé: *Corros. Sci.*, 2004, vol. 46, pp. 1401–29.
34. M. Yamashita, H. Miyuki, Y. Matsuda, H. Nagano, and T. Misawa: *Corros. Sci.*, 1994, vol. 36, pp. 283–99.
35. T. Kamimura, S. Hara, H. Miyuki, M. Yamashita, and H. Uchida: *Corros. Sci.*, 2006, vol. 48, pp. 2799–12.
36. ASTM Committee: *Report No. B117-18, ASTM International*, (West Conshohocken, PA), 2003.
37. P.K. Katiyar, S. Misra, and K. Mondal: *Metall. Mater. Trans. A*, 2019, vol. 50A, pp. 1489–01.
38. P.K. Katiyar, P.K. Behera, S. Misra, and K. Mondal: *Met. Mater. Int.*, 2019, vol. 25, pp. 1209–26.
39. BIS committee: *Report No. IS: 1608*, (Bureau of Indian Standards, New Delhi, India), 2005.
40. W.D. Callister, Jr and D.G. Rethwisch: *Materials science and engineering*, 8th ed., John Wiley Sons Inc, New York, 2009.
41. E. Gadalińska, A. Baczmański, C. Braham, G. Gonzalez, H. Sidhom, S. Wroński, T. Buslaps, and K. Wierzbanowski: *Int. J. Plast*, 2020, vol. 127, p. 102651.
42. S. Sharma, S. Sangal, and K. Mondal: *Metall. Mater. Trans. A*, 2014, vol. 45A, pp. 6088–02.
43. ASTM Committee: Report No. G102-89, (ASTM International West Conshohocken, PA), 2016.
44. J. Shi and J. Ming: *Int. J. Miner. Metall. Mater.*, 2017, vol. 24, pp. 64–74.
45. J. Shi, J. Ming, and W. Sun: *J. Mater. Civ. Eng.*, 2018, vol. 30, p. 04018212.
46. L. Veleva: *Corrosion Tests and Standards: Application and Interpretation*, second edition (edited by R. Baboian; Section Editor: H.P. Hack), ASTM International, Pennsylvania, January 2005, page 392.
47. J.A.S. Greene and R.N. Parkins: *Corrosion*, 1968, vol. 24, pp. 66–69.
48. A.J. Bard and L.R. Faulkner: *Electrochemical methods: fundamentals and applications*, 2nd ed., John Wiley Sons Inc, New York, 2001.
49. A.H. Cottrell and B.A. Bilby: *Proc. Phys. Soc. Section A*, 1949, vol. 62, pp. 49–62.
50. C.W. Richards: *Engineering materials science*, 2nd ed., Chapman and Hall, Wardsworth Publishing Company, London, 1968.
51. T. Wu, M. Yan, J. Xu, Y. Liu, C. Sun, and W. Ke: *Corros. Sci.*, 2016, vol. 108, pp. 160–68.
52. Y. Wang, W. Zhao, H. Ai, X. Zhou, and T. Zhang: *Corros. Sci.*, 2011, vol. 53, pp. 2761–66.
53. L.Y. Xu and Y.F. Cheng: *Corros. Sci.*, 2012, vol. 64, pp. 145–52.
54. E.M. Gutman: *Mechanochemistry of materials*, Cambridge International Science Publication, Cambridge, U.K., 1998.
55. R. Balasubramaniam, A.V. Ramesh Kumar, and P. Dillmann: *Curr. Sci.*, 2003, vol. 85, pp. 1546–55.
56. T. Misawa, K. Asami, K. Hashimoto, and S. Shimodaira: *Corros. Sci.*, 1974, vol. 14, pp. 279–89.
57. M. Stratmann, K. Bohnenkamp, and H.J. Engell: *Corros. Sci.*, 1983, vol. 23, pp. 969–85.
58. A. Raman, S. Nasrazadani, and L. Sharma: *Metallography*, 1989, vol. 22, pp. 79–96.
59. K. Xiao, C. Dong, X. Li, and F. Wang: *J. Iron Steel Res. Int.*, 2008, vol. 15, pp. 42–48.
60. X. Zhang, S. Yang, W. Zhang, H. Guo, and X. He: *Corros. Sci.*, 2014, vol. 82, pp. 165–72.
61. L.T. Mammoliti, L.C. Brown, C.M. Hansson, and B.B. Hope: *Cem. Concr. Res.*, 1996, vol. 26, pp. 551–56.
62. H. Bensabra and S. Belkhair: *Alg. J. Mat. Chem.*, 2018, vol. 1, pp. 16–28.
63. J. Ahlström, J. Tidblad, L. Tang, B. Sederholm, and S. Leijonmarck: *Int. J. Corros.*, 2018, vol. 2, p. 5623504.
64. J. Avila-Mendoza, J.M. Flores, and U.C. Castillo: *Corrosion*, 1994, vol. 50, pp. 879–85.